

Chemical &  
Molecular  
Engineering

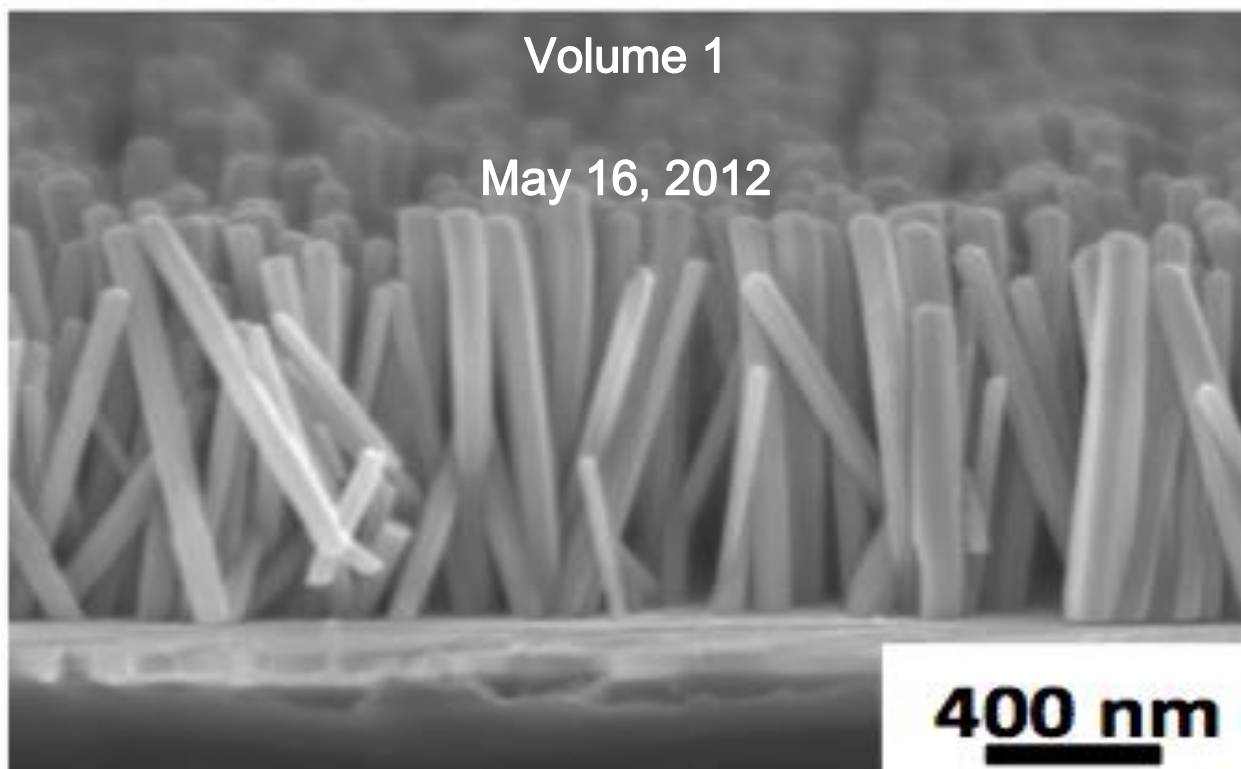
— AT STONY BROOK UNIVERSITY —

# JUCER

Journal for Undergraduate Chemical Engineering Research

Volume 1

May 16, 2012



**400 nm**

# JUCER

Journal for Undergraduate Chemical Engineering Research

JUCER is a journal dedicated to highlighting undergraduate research in chemical engineering. The articles in this volume were peer reviewed and edited by the graduating seniors of the class of 2012.

- ✧ **Editor in Chief : Marie Guevarra**
  
- ✧ **Associate Editors : Sung Bong Tae, Byoung Su Kim, Kyu dong Noh,  
Jim Chen, Joseph Imbrogno, Jovan Kamcev,  
Chang Hoon Lee, Rui Lin Tan, Sung Hoon Kim,  
Yong Hee Kim, Minkyu Park, Zhenghao Li,  
James Messina**

**Volume I**

**May 16, 2012**

# JUCER

Journal for Undergraduate Chemical Engineering Research

## Table of Contents

<b>Polypropylene Nanocomposites Suitable for Heat Exchangers</b> ChangHoon Lee, James Messina, Minkyu Park, Kai Yang, Miriam Rafailovich, Thomas Butcher, Rebecca Trojanowski	<b>Page 1</b>
<b>Do Bone Cells Still Have Their Primary Cilia?</b> Marie Guevarra , Kathryn Dorst, Yizhi Meng	<b>Page 9</b>
<b>Band-Gap-Engineered Solution-Synthesized Vertical Zinc Oxide Nanowire Arrays for Light Harvesting Applications</b> Jovan Kamcev and Chang-Yong Nam	<b>Page 13</b>
<b>Molecular Dynamics Simulation of Dissociation Kinetics and Vibrational Energy Distribution</b> Rui Tan	<b>Page 20</b>
<b>Model Drug Delivery System Using Gelatin Microspheres</b> Zhenghao Li, Xin He, Yizhi Meng	<b>Page 28</b>
<b>Exploration of the Relationship between Microscopic Structures and Macroscopic Properties of Biodiesel to Improve its Efficiency as a Future Energy Source</b> Joseph Imbrogno, Sung Bong Tae, Tadanori Koga, Keith Jones	<b>Page 35</b>

# Polypropylene Nanocomposites Suitable for Heat Exchangers

ChangHoon Lee<sup>1</sup>, James Messina<sup>1</sup>, Minkyu Park<sup>1</sup>, Kai Yang<sup>1</sup>, Miriam Rafailovich<sup>1</sup>, Thomas Butcher<sup>2</sup>, Rebecca Trojanowski<sup>2</sup>

<sup>1</sup> Department of Material Science and Engineering, Stony Brook University, NY 11794  
(Program in Chemical and Molecular Engineering)

<sup>2</sup> Brookhaven National Laboratory, Department of Energy, Upton, NY 11973

---

## Article Information

*Keywords: Name [abbrev]*

Polypropylene [PP]

Mixture [PRA]:

<sup>1</sup>PBrS (Brominated polystyrene)

<sup>2</sup>RDP Clay

<sup>3</sup>Antimony trioxide

Al(OH)<sub>3</sub> [ATH]

Mg(OH)<sub>2</sub> [MDH]

Multi-walled Carbon Nanotube [CNT]

Multi-layered Graphene [Graphite]

Thermal Conductivity

Flame Retardancy

Young's Modulus [E]

Scanning Electron Micrograph [SEM]

---

## Abstract

The increase of thermal conductivity and flame-retardant behavior was obtained by incorporating flame retardant ATH, MDH, PRA, and very high thermal conductivity CNT fillers into a polypropylene matrix. The results showed that CNT, ATH, and MDH fillers have influences on thermal conductivity. ATH, MDH, and mixture fillers also greatly improved the flame retardancy as well. However due to fillers, yield strength at the break point of the polymer composites decreased and Young's Modulus increased. The major goal of this trial and error experiment was to produce composites suitable for heat exchanger applications. The most favorable combination was the blend of these three fillers: 30% ATH, 20% MDH, 10% CNT, and 40% PP in wt%, giving total of 50 grams. The thermal conductivity was 1.1 W/m K, increasing the thermal conductivity of the PP composite to 10 times higher than the pure PP. UL-94 vertical burning test ranking was V-0. Young's Modulus at the break point was 21.0 MPa, with a yield strength of 28.2 MPa.

---

## 1. Introduction

The amount of heat energy lost to the environment during the operation of conventional gas-fired boilers and/or furnaces can be recovered by using condensing heat exchangers [1]. However, due to the chemically harsh environment of the exit flue gas, which includes the condensation of nitric acid, sulfuric acid, and hydrochloric acid, corrosion occurs on the metal alloys that are used for the heat exchanger. The high expense of corrosion-resistant metal alloys outweighs the materials' usefulness [2]. Therefore, a great deal of research has gone into investigating the use of polymer composites as alternate construction materials of heat exchangers, in contrast to conventional metal alloys.

Not only are polymers significantly lighter in weight and much cheaper, but they also are

very easy mold into desired shapes for many designs. In order for polymers to be used as a viable heat-exchanger construction material, the limitations that are inherent to most natural polymers must be overcome. Most common polymers have a thermal conductivity that is only on the order of 0.1 W/m·K, which could be hundreds of times smaller than that of common metals. Additionally, many polymers perform differently in terms of chemical resistance to various acids, alkalis, and solvents [3]. Furthermore, most polymers are highly flammable and can produce toxic products during combustion [4].

Therefore, careful consideration must go into engineering a suitable composite material. A composite material is made of at least two constituents, and has characteristics that are derived

from the properties of the individual constituents [3]. The matrix is the material present in the continuous phase, which is usually, but not always, present in the greatest quantity [3]. The remaining constituents, or fillers, are in the reinforcing phase, and are used to enhance the properties of the matrix [5]. These reinforcements can include flame-retardants, which alter the combustion behavior of polymers at ignition temperatures, and can also include particulates that modify other properties such as thermal conductivity and tensile yield strength.

The material must be able to withstand high-temperature operating conditions and be safe to the user. Thus, it must be engineered to be flame-retardant, have enough yield strength and lastly achieving the primary objective of having an increased thermal conductivity. This objective was to be achieved by a trial-and-error experiment. Polypropylene (PP) was used as a polymer matrix, mainly due to its corrosion resistance. The fillers that were used included aluminum trihydroxide (ATH), magnesium dihydroxide (MDH), carbon nanotubes (CNT), and a mixture consisting brominated polystyrene, RDP clay, and antimony trioxide; this mixture is collectively abbreviated as "PRA."

## 2. Materials and Procedures

### 2.1 Instruments

\*All measurements were measured with a Vernier caliper with an error of  $\pm 0.0005$  cm.

### Melt-Blending

For mixing the polymer composites, a C.W. Brabender Intelli-Torque Plasti-Corder® torque rheometer was used. The components were poured into the unit's mixing bowl, the polymer being first. Once all of the composites have been added into the melted polymer, the unit was closed and the drive speed was increased to ensure even distribution throughout the polymer. The mixer ran for at least ten minutes. The blending was then stopped and the mixture was cooled until it hardened, allowing for easier removal from the machine.

### Heat Press Molding

The collected polymer composite was broken up into tiny pieces and placed into metal plates with the metal mold pieces of various shapes and sizes used for different elements of testing. The polymer composite in the metal mold piece was placed upon a steel plate covered in *Kapton*® film, with another layer of film and another steel plate placed on top. The plates were then placed in a Carver® Model C heat press for molding. Great care was taken to ensure that the molds were completely filled and to minimize the presence of air bubbles.

### Thermal Conductivity Test

The block samples had dimensions of 5.125 cm x 5.001 cm x 1.096 cm in length, width, and thickness, respectively. The thermal conductivity was measured using a QTM-500 (Quick Thermal Conductivity Meter). This test was done in Brookhaven Laboratory by Department of Energy faculty.

### UL-94 Vertical Flame Test

With sample dimensions of 12.165 cm x 1.300 cm x 0.500 cm in length, width, and thickness, respectively, this test measures the ignition rate of polymer composites. It was burned vertically upward with a tester.

The most widely used standard in classifying materials as flame-retardant is UL 94, established by Underwriters Laboratories. In this experiment, the UL 94 V flame test was carried out with composite samples that were specifically molded for ignition testing. There are three main classifications of flame-retardant materials in the UL-94 standard: V-0, V-1, and V-2. In the UL 94 V flame test, a 20mm-high flame with a power of 50 W is applied to the bottom of a material sample in the vertical position, within a chemical fume hood [4]. The classification according to the UL-94 standard is listed on **Table 1**. Throughout the test, a piece of cotton is kept under the sample. This is done in order to see if flaming droplets from the

sample cause the cotton to ignite; this is the difference between a V-1 and V-2 classification.

**Table 1 [6]**

Classifications according to the UL-94 standard.

Ranking	Description
HB	Slow burning on a horizontal specimen; burning rate <76 mm/ min for thickness <3 mm.
V-2	Burning stops within 30 s on a vertical specimen; drips of flaming particles are allowed.
V-1	Burning stops within 30 s on a vertical specimen; drips of particles are allowed as long as they are not inflamed.
V-0	Burning stops within 10 s on a vertical specimen; drips of particles are allowed as long as they are not inflamed.

### Yield Strength Test

For the yield strength test, an Instron® 5542 tensile tester was used. The samples were molded into a “dog bone” shape with a length and thickness of 8.043cm and 0.158cm, respectively. They were then placed in two clamps that pulled the samples in opposing directions until they broke.

### *2.2 Materials Preparation*

As the polymer matrix, PP was used for its corrosion resistance. PP was obtained from Company TOTAL, fine powders of ATH and MDH were obtained from J.M. Huber Corporation, and CNT was obtained from Cheap Tubes® with purity greater than 98%. Lastly, PRA was prepared at Stony Brook University. The characterization of the polymer and fillers are listed on **Table 3**, excluding PRA filler. This experiment was essentially a trial and error experiment to determine the optimum combination for the PP composite.

First trial: The weight of each PRA mixture was measured; the optimum combination for the flame retardant was 14% PBrS, 10% RDP Clay, and 3% antimony trioxide [10]. Then, 4% CNT and PRA fillers were mixed thoroughly into the PP. Excluding all the fillers, PP itself measured 69% in wt%, giving the total of 100% after the addition of CNT and PRA fillers. Then, this **Mixture1** was

melt-blended and molded into several shapes and sizes for tests.

Later, Cool Polymers® donated an E2 series sample. It was ignited into powder in order to observe the residues by using SEM. **Figure 2** shows the presence of some metal particles with high concentrations of carbon particles.

Second trial: **Mixture2** of 50% ATH and 50% PP was melt-blended and molded into various shapes and sizes for tests.

Third trial: **Mixture3** of 40% MDH and 60% PP was melt-blended and molded into various shapes and sizes for tests.

Fourth trial: **Mixture4** of 30% ATH, 20% MDH, and 50% PP was melt-blended and molded into various shapes for tests.

Final trial: **Mixture5** of 50% ATH, 10% CNT, and 40% PP was prepared. **Mixture6** of 30% ATH, 20% MDH, 10% CNT, and 40% PP was prepared. These mixtures were melt-blended and molded into various shapes for tests. SEM images were collected for these two mixtures.

\* The data were analyzed at the end of each trial.

## **3. Results**

### *3.1 First Trial Mixture1*

Ignition Test: Fire extinguished after 4 seconds of burning with no drips. It achieved V-0.

Thermal Conductivity Test: The thermal conductivity value came out to be 0.41 W/m·K, which was still too low.

### *3.2 Second Trial Mixture2*

Ignition Test: Fire extinguished after 8 seconds of burning without drips. However, it achieved V-0.

Thermal Conductivity Test: The thermal conductivity value came out to be 0.62 W/m·K. It was still relatively low.

### 3.3 Third Trial **Mixture3**

Ignition Test: Fire did not extinguish but rather was burning very slowly with no drips.

### 3.4 Fourth Trial **Mixture4**

Ignition Test: Fire extinguished within 2 seconds of burning without drips. It achieved V-0.

Thermal Conductivity Test: The thermal conductivity value came out to be 0.71 W/m·K. It was still relatively low, but better.

### 3.5 Fifth Trial (Optimum Combination)

#### (**Mixture5 and Mixture6**)

Ignition Test for **Mixture5**: Fire extinguished after 6 seconds of burning without drips. It achieved V-0.

Thermal Conductivity of **Mixture5**: The thermal conductivity value came out to be 1.01 W/m·K. This is almost 10 times higher than the thermal conductivity for just pure PP.

Tensile Test: Yield strength at the break point was 27.2 MPa. E = 20.3 MPa.

Ignition Test for **Mixture6**: Fire extinguished after 2 seconds of burning without drips. It achieved V-0.

Thermal Conductivity of **Mixture6**: The thermal conductivity value came out to be 1.1 W/m·K. This is 10 times the increase compared to the thermal conductivity of pure PP.

Tensile Test: Yield strength at the break point was 28.2 MPa. E = 21.0 MPa.

**Table 2**  
Results Summary

Mixture #	Ignition Test	Thermal Conductivity	Tensile Test
1	V-0 (4 seconds)	0.41 W/m·K	N/A
2	V-0 (8 seconds)	0.62 W/m·K	N/A
3	Did not extinguish	N/A	N/A
4	V-0 (2 seconds)	0.71 W/m·K	N/A
5	V-0 (6 seconds)	1.01 W/m·K	Yield strength: 27.2 MPa E = 20.3 MPa
6	V-0 (2 seconds)	1.1 W/m·K	Yield strength: 28.2 MPa E = 21.0 MPa

**Table 3**  
Properties of PP and its fillers.

Property	PP	CNT	MDH	ATH
Thermal Conductivity (W/m K)	0.12	1.52 - 7000 [7], [17]	0.131 - 0.213	10 - 30
Density (g/cm <sup>3</sup> )	0.85	-----	2.34	2.42
Mean particle diameter (µm)	-----	3000 - 30000 [8]	0.5 - 1.5	5

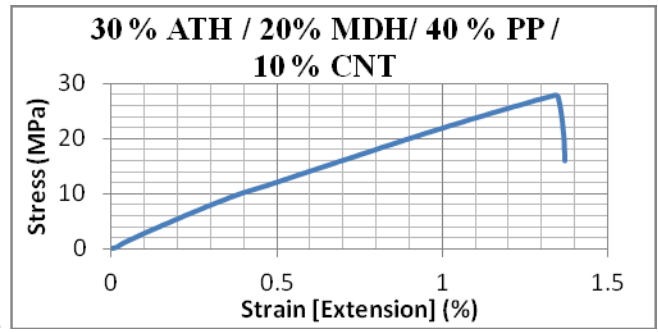
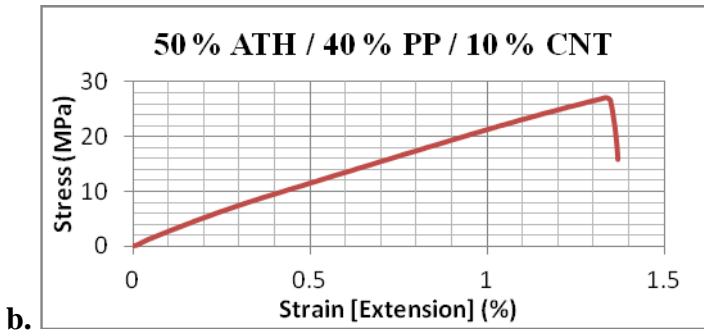
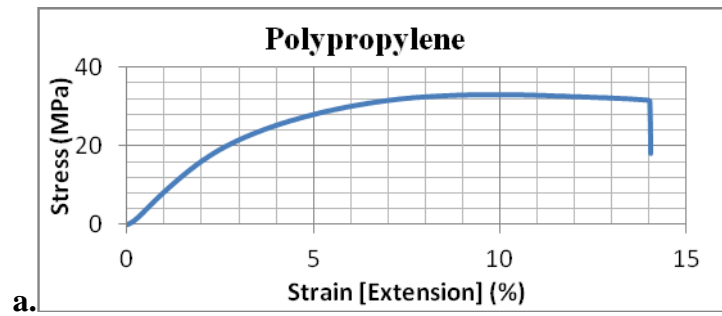


**Figure 1. a.** Tensile test for pure PP. Yield Strength at the break point is about 31.9 MPa.  $E = 2.3 \text{ MPa}$  **b.** Tensile test for **Mixture5**. **c.** Tensile test for **Mixture6**.

3.6 SEM images for E2 Sample, **Mixture5**, and **Mixture6**.

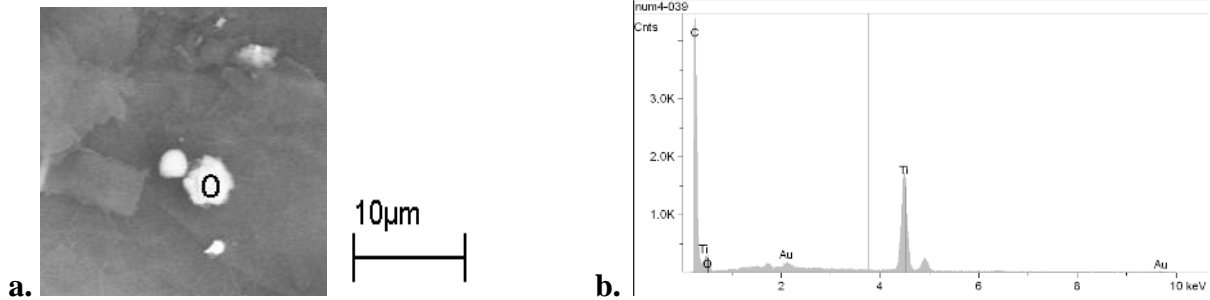


**Figure 2.** SEM images of E2 Sample.

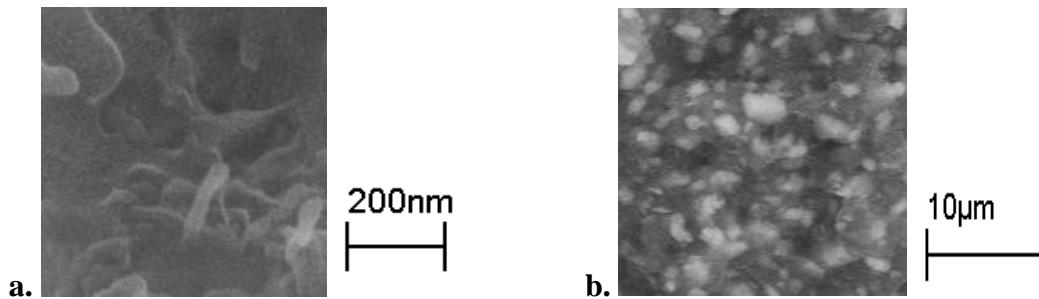


**Figure 3.** SEM images of **Mixture5** (40% PP / 50% ATH / 10% CNT).

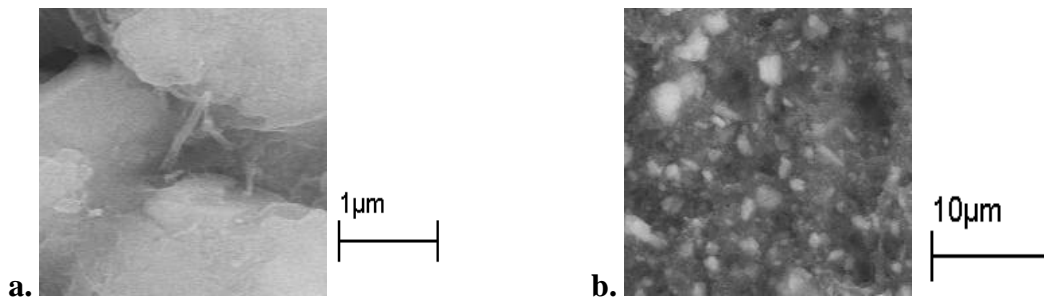


**Figure 4.** SEM images of **Mixture6** (40% PP / 30% ATH / 20% MDH / 10% CNT).

#### 4. Discussion

As mentioned previously, the main objective of this research was to produce a PP composite with higher thermal conductivity and flame-retardancy. Therefore, CNT, PRA, ATH, MDH were chosen for the fillers. PRA, ATH and MDH are renowned for flame retardancy, and CNT is widely renowned for high thermal conductivity with strong tensile strength of 13 – 53 GPa. It is the strongest material ever tested, after graphene and diamonds, which are different forms of carbon. Graphene is the basic structural element of several allotropes, including CNT, fullerenes and graphite. Many graphene sheets stacked on top of each other is called multi-layered graphene, aka graphite. CNT is the cylindrical form, and fullerene is the spherical form of the graphene. Thermal conductivity of graphene depends on the numbers of layers, With a high amount of layers, the thermal conductivity is about 1000 W/m K at 8 atomic planes [7]. The thermal conductivity of CNT is mostly similar to graphene but varies heavily depending on conditions. These include the thickness, number of layers, concentration, arrangement of bundles, length and diameter, temperature, and whether the thermal conductivity was measured along or across the axial plane[7], [16], [17]. Thermal conductivity can range from 1.52 W/m K to 3500 W/m K and much more for single-walled carbon nanotubes. Since single layered graphene with just one atom layer was not obtainable, CNT was used [16], [17].

For the first trial, we expected little increase in thermal conductivity, since the PRA flame

retardant reduces the heat exchange between the surface and the bulk. When the surface temperature increases rapidly, time required for the bulk to reach the pyrolysis temperature is drastically decreased [9]. While searching for alternative flame retardant composites, we were able to obtain a sample E2. This sample includes PP as the matrix and many other composites, mostly carbon and some titanium (Ti). The circled particle is the Ti on **Figure 2**.

Therefore, Titanium dioxide ( $\text{TiO}_2$ ) was an alternative particle. However,  $\text{TiO}_2$  barely increased the thermal conductivity [11]. So instead, ATH was chosen for the reinforcing phase. 50% ATH (the rest PP) showed improved results, with V-0 and a thermal conductivity value of 0.62 W/m·K. ATH works as a mineral flame-retardant by undergoing an endothermic chemical reaction. Between 180 and 200 °C, ATH decomposes to form alumina ( $\text{Al}_2\text{O}_3$ ) and water vapor:  $2\text{Al}(\text{OH})_3 \rightarrow \text{Al}_2\text{O}_3 + 3\text{H}_2\text{O}$  (1050 kJ/kg) [4]. During combustion, the absorption of energy by ATH cools down the matrix material (ie. polypropylene), the alumina “forms a thermally insulating protective coating” [4] around the polymer, and “the released water vapor dilutes combustible gases and forms a protective gas layer” [4] around the polymer, thus preventing the spread of flames. For ATH to be effective as a flame-retardant in a polymer material, it must be present in a high loading level [4]. Therefore, the loading levels of ATH used in composites made for this experiment was 50% by mass. ATH is also a conductive particle, so the increase of thermal conductivity was expected.

Another flame retardant mineral was MDH. It degrades endothermically at a higher temperature

than ATH (300 °C) and is suitable for use up to a temperature of 400 °C, where its degradation becomes exothermic instead [4]. The diameter of MDH is smaller compared to ATH. The bigger the diameter of the particle is, the smaller the Oxygen Index (OI), and vice versa [12]. The smaller the particle is, the greater the specific surface area of the flame is, improving the flame-retardant behavior by slowing down the ignition. When MDH was blended into the PP, it did not give V-0, but rather, it slowed down the burning rate dramatically. ATH alone blended into PP gave a V-0 rating, within 8 seconds of burning. Therefore, the mixture of ATH and MDH would result in V-0 much faster than the ATH alone. As the result, the flame extinguished within 2 seconds of burning and yielded a thermal conductivity of 0.71 W/m·K.

After achieving a V-0 PP composite, CNT were inserted into each mixture of **Mixture2** and **Mixture4**, resulting in **Mixture5** and **Mixture6**, respectively. V-0 was maintained, with only 2 seconds of burning. Even with CNT, the increase of thermal conductivity was little, giving the results of 1.01 and 1.1 W/m·K for **Mixture5** and **Mixture6**, respectively. Comparing to the thermal conductivity value of pure PP, **Mixture6** elevated the thermal conductivity value by approximately 10 times. The reason that CNT had little effect on the thermal conductivity is because the thermal conductivity of CNT heavily depends on whether the thermal conductivity is measured along or across the axial direction, not only on the number of layers and bundles [7], [12].

When the tensile test results of **Mixture5**, **Mixture6**, and pure PP were compared, Young's Modulus for **Mixture5** and **Mixture6** has increased tremendously. The composites were very brittle due to the amounts of fillers that were used. However, the yield strengths at the break point for **Mixture5** and **Mixture6** decreased by about only 4 MPa compared to the pure PP. **Mixture6** had a slightly higher yield strength at the break point due to the small diameter of MDH, as well as MDH's density, which is slightly lower than ATH. The particle size and density affect the mechanical properties of the composite [14], [15].

The tentacle-like particle on left side of **Figure 3** shows the carbon nanotubes. In the image on the right, the particles are the ATH. In **Figure 4**, the tentacle-like image on the left is also the CNT. On the right, it is difficult to figure out whether the particles are ATH or MDH.

## 5. Conclusion

Thermal conductivities, UL-94 standard rankings, and tensile tests were determined for PP composites using PRA, ATH, and MDH. From the results, PRA achieved a UL-94 ranking of V-0. Not only did ATH and MDH work very well on extinguishing the flame, but they also increased the thermal conductivities. Even though positive effects resulted because of these two properties, a lot of ATH and MDH had to be consumed in order to obtain these results. Due to the fact that a lot of fillers had to be consumed, it decreased the yield strength at the break point by approximately 4 MPa for **Mixture5** and **Mixture6**, compared to pure PP. So far, **Mixture6** with 30% ATH, 20% MDH, 10% CNT, and 40% PP, had the optimum combination. The results were a UL-94 ranking of V-0, fire extinguishing within 2 seconds, and thermal conductivity value of 1.1 W/m·K. Therefore, our next challenge is to produce a polymer composite with as little fillers as possible and to bring out the maximum properties from the CNT while maintaining a UL-94 ranking of V-0. Even though much work still needs to be done, this composite shows potential for future research.

## References

- [1] Che, Defu, Yanhua Liu, and Chunyang Gao. "Evaluation of Retrofitting a Conventional Natural Gas Fired Boiler into a Condensing Boiler." *Energy Conversion & Management* 45 (Mar. 2004): 3251-3266. Elsevier. Web. July 2010. <<http://www.elsevier.com/locate/enconman>>.
- [2] Bigg, D. M., G. H. Stickford, and S. G. Talbert. "Applications of Polymeric Materials for Condensing Heat Exchangers." *Polymer Engineering and Science* 29.16 (1989): 1111-1116. Print.
- [3] T'Joen, C., et al. "A Review on Polymer Heat Exchangers for HVAC&R Applications." *International Journal of Refrigeration* 32.5 (2009): 763-779. Elsevier. Web. 27 Sept. 2011. <[www.elsevier.com/locate/ijrefrig](http://www.elsevier.com/locate/ijrefrig)>.
- [4] Laoutid, F., L. Bonnaud, M. Alexandre, J.-M. Lopez-Cuesta, Ph. Dubois, "New Prospects in Flame Retardant Polymer Materials: From Fundamentals to Nanocomposites." *Materials Science and Engineering: R: Reports*, 63.3 (29 January 2009): 100-125. <<http://www.sciencedirect.com/science/article/pii/S0927796X08000892>>.
- [5] Gurdal, Z., Haftka, R.T., Hajela, P., 1999. Wiley. "Design and Optimization of Laminated Composite Materials." New York.
- [6] Shi, Zhixiang, Renli Fu, Simeon Agathopoulos, Xiguang Gu, and Weiwei Zhao. "Thermal Conductivity and Fire Resistance of Epoxy Molding Compounds Filled with Si<sub>3</sub>N<sub>4</sub> and Al(OH)<sub>3</sub>." *Materials & Design* (2011). Print.
- [7] Balandin, Alexander A. "Thermal Properties of Graphene and Nanostructured Carbon Materials." *Nature Materials* (2011). Print.
- [8] "Multi-wall Nanotubes (MWNT)." *Nanocyl*. Web. 01 May 2012. <<http://www.nanocyl.com/en/CNT-Expertise-Centre/Carbon-Nanotubes/Multi-wall-Nanotubes-MWNT>>.
- [9] "Fire Retardancy of Polymers." *Google Books*. Web. 01 May 2012. <<http://books.google.com/books?id=U02HtkqSCLYC>>.
- [10] Rafailovich, Miriam H., et al. "Thermally Stable and Flame Retardant Polymer Nanocomposites." (2011). Print.
- [11] Agrawal, Sonam. "Effective Thermal Conductivity of Epoxy Matrix Composites Filled with Titania (TiO<sub>2</sub>) Powder" (2011). Print.
- [12] Liang, Jizhao, and Yingjie Zhang. "A Study of the Flame-retardant Properties of Polypropylene/Al(OH)<sub>3</sub>/Mg(OH)<sub>2</sub> Composites" (2009). Print.
- [13] Evans, William J., and Pawel Keblinski. "Thermal Conductivity of Carbon Nanotube Cross-bar Structures." *Nanotechnology* 21.47 (2010): 475704. Print.
- [14] Mai, Kancheng, Zhengjun Li, Yuxin Qiu, and Hanmin Zeng. "Physical and Mechanical Properties of Al(OH)<sub>3</sub>/polypropylene Composites Modified by in situ-functionalized Polypropylene." *Journal of Applied Polymer Science* 83.13 (2002): 2850-857. Print.
- [15] E., Eichie F. "Effect of Particle Size of Granules on Some Mechanical Properties of Paracetamol Tablets." *African Journal of Biotechnology* 8 (21) (2009): 5913-916. Print.
- [16] Mann, David; Wang, Qian; Goodson, Kenneth; Dai, Hongjie. "Thermal Conductance of an Individual Single-wall Carbon Nanotube Above Room Temperature". *Nano Letters* 6 (1): 96-100.
- [17] Sinha. Saion, Barjami. Saimir, Iannacchione. Germano, Schwab. Alexander, Muench. George, "Off-axis Thermal Properties of Carbon Nanotube Films". *Journal of Nanoparticle Research* 7 (6): 651-657.

# Do bone cells still have their primary cilia?

Marie Guevarra<sup>1</sup>, Kathryn Dorst<sup>2</sup>, Yizhi Meng<sup>1,2</sup>

<sup>1</sup> Program in Chemical and Molecular Engineering, Stony Brook University, NY

<sup>2</sup> Department of Materials Science Engineering, Stony Brook University, NY

---

## ABSTRACT

Defective primary cilia are known to be one of the causes of human diseases and developmental disorders. Detecting it and finding what cell lines has a defective primary cilia is important. While primary cilia have emerged as a critical component of diverse signaling transduction complexes, little is known about its presence in bone cells. Here we focused on studying the presence or absence of primary cilia of two pre-osteoblast cell lines (MC3T3-E1 subclone 4 and 24) and a rat osteosarcoma cell line (ROS 17/2.8) using immunofluorescence microscopy and measure their average cilia length. It was determined that MC3T3-E1 subclone 4 has the greatest percent of cilia occurrence (68 %), while the ROS cell line showed the least cilia occurrence (17%). Sub 4 and 24 showed a normal average cilia length, whereas the ROS cilia is depleted. This study represents preliminary data for future, more qualitative experiment.

*Keywords: cell migration, primary cilia*

---

## 1. Introduction

The primary cilia of a cell was recently elucidated as a major site for diverse signaling pathways because of a variety of receptors, ion channels and transporter proteins are localized within the cilium or the basal body [2]. Its unique ultrastructure consisting of 9+0 microtubule pattern (9 peripheral doublets, no central pair of microtubule) makes is a non-motile organelle. The primary cilia usually occur singularly, emerging from the distal centriole of the centrosome of most mammalian cell and

it appears only on differentiate, growth arrested ( $G_0$  phase) cells [2]. Ciliary assembly is maintained by intraflagellar transport; a coordinated process that involves a system of motor proteins and adaptors [3]. It has been proven that primary cilia have the potential to transduce both mechanical and biochemical signals by converting them into intracellular signals that control a variety of processes, such as tissue homeostasis [4]. However, little is known

about the relationship between primary cilia and cell migration.

The purpose of this study is to determine whether or not primary cilia are present in normal differentiating pre-osteoblast cell line, non-differentiating pre-osteoblast cell line and a rat osteosarcoma cell line. It was our hypothesis that primary cilia are necessary for normal migration of the cell. We also determined the percent occurrence of primary cilia per cell lines, and determined their average cilia length.

## 2. Materials And Methods

### 2.1 Cell culturing

MC3T3-E1 subclone 4 and 24 osteoblast cells were grown in alpha Minimum Essential Media (a-MEM) and supplemented with 10% Fetal Bovine Serum (FBS) and 1% penicillin-streptomycin at 37°C, 5% CO<sub>2</sub>, 95% humidity. Rat osteosarcoma cell line (ROS 17.28) were grown in Ham's media supplemented with 10% fetal bovine serum (FBS) and 1% penicillin-streptomycin also at 37°C, 5% CO<sub>2</sub>, 95% humidity. All cell lines were grown on tissue culture plates. Cells were plated for 24h at a density of 10,000 cells/cm<sup>2</sup>.

### 2.2 Immunofluorescence Microscopy (IF)

Cells were plated at a density of 5,000 cells/cm<sup>2</sup> for 24h on a 24-well tissue culture plate and then serum starved for 48h to induce growth arrest. Cells were fixed in 4% formaldehyde, permeabilized in 0.2% triton X100 and incubated with primary antibody at room temperature

for 2h. Cells were washed twice with PBS and incubated with secondary antibody for 1h. Fluorescence were visualized using Olympus X51. Primary antibody, which attaches to the tubulin of the cells was detected with mouse acetylated alpha tubulin antibody (1:3000 Sigma T67993). The secondary, which tags the primary antibody was detected with Alexa Fluor 568 (1:600, Invitrogen A11019). Nuclei were stained with DAPI (2.5ug/ml).

### 2.3 Statistical Analysis

For two-sample comparison, a student's *t* test was used. Statistical significance was accepted at  $p < 0.05$  and data is reported as the mean  $\pm$  standard error of the mean (SEM).

## 3. Results

### 3.1 Growth Curve Data

The rate of cell replication of each cell type was studied by performing a growth curve analysis.

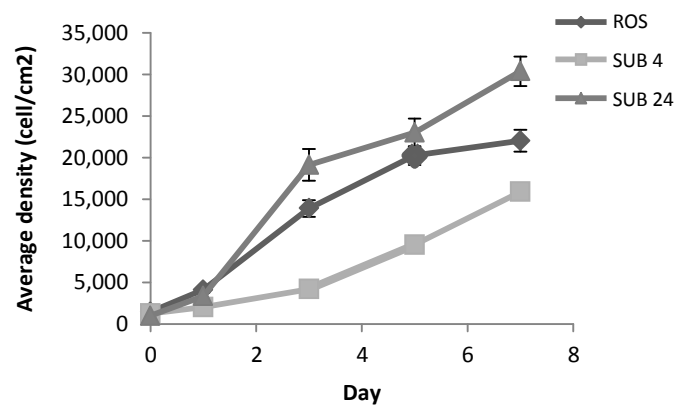


**Figure 1. Growth curve.** Growth data of MC3T3-E1 subclone 4 and 24 pre-osteoblast cells and ROS. Cells were seeded at a density of 5,000 cells/cm<sup>2</sup> in a 24 well tissue culture plate and maintained at 5% CO<sub>2</sub> (95% humidified) and 37°C. ImageJ software was used to analyze the data.

### 3.2 Immunofluorescence Staining

The primary cilia were detected using immunofluorescence staining and it was analyzed using ImageJ software.

#### Images for MC3T3-E1 subclone 4

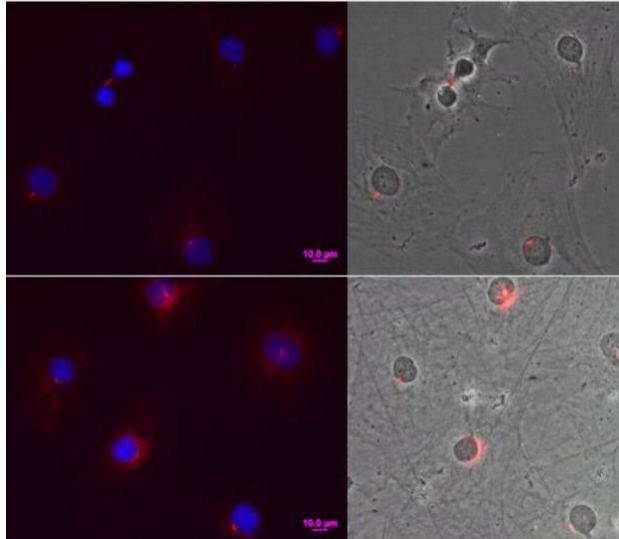


**Figure 2. Immunofluorescence staining of primary cilia in MC3T3-E1 subclone 4.** Cells were grown in 24 well tissue culture plates at a density of 5,000 cells/cm<sup>2</sup>. The primary cilia was detected using acetylated alpha-tubulin and Alexa Fluor 568. Column A: DAPI in blue, tubulin in red. Column B: phase contrast in gray, tubulin in red.

#### Image for ROS

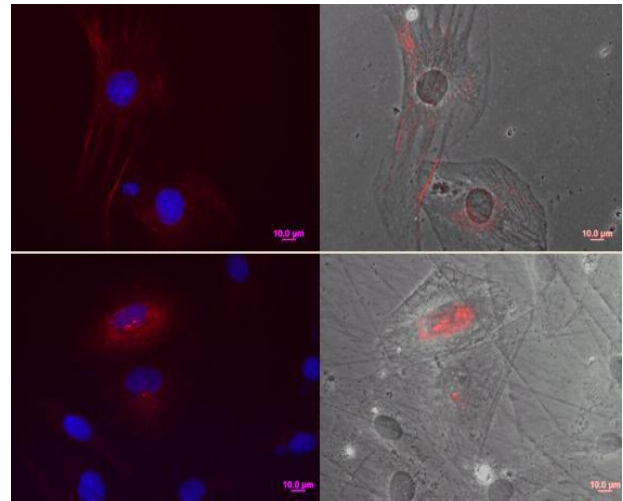


**Figure 4. Immunofluorescence staining of primary cilia in ROS osteosarcoma cell line.** Cells were grown in 24 well tissue culture plates at a density of 5,000 cells/cm<sup>2</sup>. The primary cilia was detected using acetylated alpha-tubulin and Alexa Fluor 568. Column A: DAPI in blue, tubulin in red. Column B: phase contrast in gray, tubulin in red.

#### Images for MC3T3-E1 subclone 25

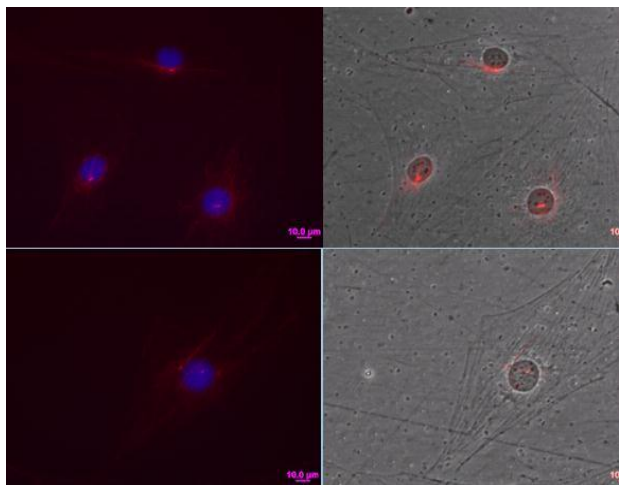


**Figure 3. Immunofluorescence staining of primary cilia in MC3T3-E1 subclone 24.** Cells were grown in 24 well tissue culture plates at a density of 5,000 cells/cm<sup>2</sup>. The primary cilia was detected using acetylated alpha-tubulin and Alexa Fluor 568. Column A: DAPI in blue, tubulin in red. Column B: phase contrast in gray, tubulin in red.

#### Percent Occurrence of Primary Cilia

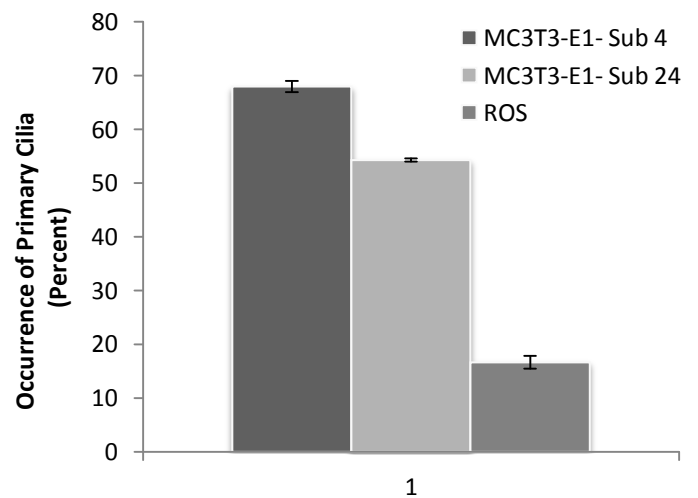


**Figure 5. Occurrence of primary cilia in percent per cell lines.** Subclone 4 shows the highest percentage of primary cilia occurrence (68%), followed by subclone 24 (57%). ROS has the lowest percentage of primary cilia occurrence (17%). The percentage was manually calculated using ImageJ software.

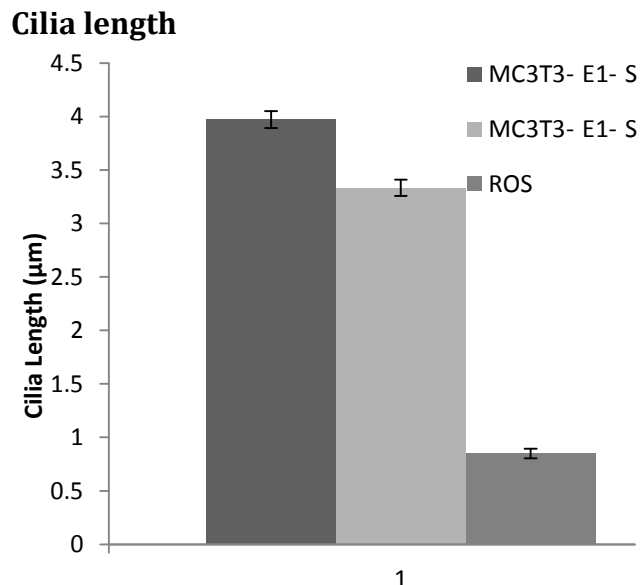


**Figure 6. Average length of primary cilia per cell line.** Subclone 4 shows the longest cilia length (3.97µm), followed by subclone 24 (3.33µm). ROS has the shortest cilia length (0.85µm). Calculations for ROS were based on the very few cilia that were present. Cilia length were manually measured using ImageJ software.

#### 4. Discussion and Conclusion

Primary cilia are seen in all three cell types. Through manual screening of the data using ImageJ software, the ROS cell line has the least percentage of primary cilia occurring as was expected. It has been shown that cancer cells either do not have primary cilia or it is defected (shorter than normal)<sup>1</sup>. Normal primary cilia length is between 3-7µm long; any length below this range is considered abnormal or defected. This result proves that cilia length is an important indication of the functions of the cell.

Both the normal pre-osteoblast cells and non-differentiating cells have a normal cilia length, 3.97 µm and 3.33 µm respectively. Both of these cell lines also have similar cilia percentage, probably because both are from the same cell line, but their main functions are different.

Additional investigation is necessary to further elucidate the reason behind this correlation. For future research, it may be beneficial to examine the role of PDGF-AA signaling pathway in cell migration.

#### 6. References

- [1] Iwaki, A. et al. *Localization and quantification of proliferating cells during rat fracture repair: detection of proliferating cell nuclear antigen by immunohistochemistry*. J. Bone Miner. Res. 1997. 12; 96-102.
- [2] Satir, P. et al., *The Primary Cilia at a Glance*. Cell Sci. 2010. 123;499-503.
- [3] Tummala, P. et al., *The Role of Primary Cilia in Mesenchymal Stem Cell Differentiation: A Pivotal Switch in Guiding Lineage Commitment*. Cell Mol Bioeng. 2010. 3(3); 207-212.
- [4] Christen ST. et al., *Sensory cilia and integration of signal transduction in human health and disease*. Traffic. 2007. 8(2); 97-109.
- [5] Ichida, M. et al., *Changes in cell migration of mesenchymal cells during osteogenic differentiation*. FEBS Letters. 2011. (585); 4018-4024.

# Band-Gap-Engineered Solution-Synthesized Vertical Zinc Oxide Nanowire Arrays for Light Harvesting Applications

<sup>1,2</sup>Jovan Kamcev and <sup>2</sup>Chang-Yong Nam

<sup>1</sup> Department of Materials Science and Engineering Program in Chemical and Molecular Engineering, Stony Brook University, Stony Brook, NY

<sup>2</sup> Center for Functional Nanomaterials Brookhaven National Laboratory, Upton, NY

---

## Abstract

In this study, we attempted the synthesis of band-gap-engineered vertical zinc oxide (ZnO) nanowire arrays using an aqueous solution growth method and solution-phase cadmium (Cd) doping. Un-doped control vertical ZnO nanowire arrays, grown on ZnO-nanocrystal-seeded indium tin oxide (ITO) substrates in aqueous Zn nitrate and hexamethylenetetramine precursor solution, had a hexagonal wurtzite structure with typical diameter ~20-40 nm and length ~0.4-1.3  $\mu$ m, which could be controlled by growth temperature and time. The Cd doping of the nanowire arrays was achieved by adding 20-30% of Zn nitrate in the growth solution and elevating the growth temperature up to ~120 °C. Optical absorption spectrum confirmed increasing red shift of band gap absorption edge up to ~10 nm with increasing growth temperature. Finally, we tested the feasibility of ZnO nanowire arrays as efficient charge collectors in inverted organic solar cells having a blend of poly (3-hexylthiophene) (P3HT) and phenyl-C<sub>61</sub>-butyric acid methyl ester (PCBM) as an active layer. On average, the ZnO charge collectors improved photovoltaic device efficiency by ~67% compared with the control devices mainly by increasing the device fill factor.

*Keywords:* Zinc Oxide Nanowires, Cadmium Doping, Photovoltaic Devices, ZnO Charge Collector

---

## Introduction

Zinc oxide (ZnO) is a wide band gap (~3.37 eV) semiconductor with attractive material characteristics such as good optical transparency, high electron mobility, environmental stability, and strong room temperature luminescence. As one-dimensional nanostructures, ZnO nanowires can exhibit further enhanced physical properties including efficient directional charge transport, increased light scattering, and large surface-to-volume ratio. ZnO nanostructures are used in a wide range of applications such as light emitting diodes<sup>1</sup>, photodiodes<sup>2</sup>, acoustic wave filters<sup>3</sup>, gas sensors<sup>4</sup>, piezoelectric devices<sup>5</sup>, and solar cells<sup>6</sup>. Despite their successful usage as an electron collector, ZnO nanowires display limited functionality in light absorption due to the large band gap and subsequently insignificant solar spectrum coverage.

Reducing the band gap of ZnO nanowires would provide important opportunities to further improved performance of ZnO-nanowire-based light harvesting applications such as hybrid solar cells and photocatalysts. Chu et al.<sup>7</sup> have previously achieved cadmium (Cd) doping in ZnO nanowires through Chemical Vapor Deposition techniques, reducing the band gap of the Cd doped nanowires to 2.08 eV. In this study, we attempted the synthesis of band-gap-reduced vertical ZnO nanowire arrays using an aqueous solution growth method and solution-phase Cd doping. Lastly, we demonstrate the usefulness of ZnO nanowires as charge collectors in inverted photovoltaic devices.

## Materials and Methods

*ZnO nanowire growth:* Indium-tin oxide substrates were cleaned by sonicating in ethanol/acetone

solution, 1M HCl solution, ethanol solution, and rinsing in ethanol followed by drying in a stream of nitrogen. The ITO substrate was seeded by placing 5-6 drops of 0.01 M zinc acetate dehydrate solution (in ethanol), waiting 12-15 seconds, rinsing with ethanol followed by drying in a stream of nitrogen, and repeating 5 times. The seeded substrate was placed on a hot plate for 20 minutes at 325 °C. The substrate was then placed in a growth solution (25mM zinc nitrate hexahydrate, 25mM hexamethylenetetramine, DI water) for varied amount of time and varied temperature.

*Organic Photovoltaic Device Fabrication:* ITO substrate containing ZnO nanowires was coated with 20 nm layer of titanium dioxide by atomic layer deposition technique. A blend of P3HT:PCBM was spin coated on top of the substrate at 3K rpm for 45 seconds. The substrate was subject to solvent annealing in sealed fluoroware container. A blend of Poly(3,4-ethylenedioxythiophene) poly(styrenesulfonate) (PEDOT:PSS) was spin coated on top of substrate at 3K rpm for 45 seconds. A layer of gold contact was deposited on top of the substrate by physical vapor deposition technique.

## Results/Discussion

The aqueous growth solution method is a bottom up approach that originated from theoretical modeling of the water-oxide interfacial thermodynamics and kinetics of nucleation, growth, and aging processes<sup>8</sup>. This aqueous method of ZnO nanowire growth is a low temperature method that essentially features two main steps: seeding the substrate and aqueous growth of nanowires. ZnO seeding prior to aqueous nanowire growth provides nucleation sites for ZnO nanowire growth and is done in a separate step in order to better control the properties of the seeding layer. ZnO seeding is accomplished through the thermal decomposition of zinc salts, in particular zinc acetate, at high temperatures in air to give zinc oxide islands with their plane perpendicular to the substrate. The orientation of the ZnO islands is independent of the type or crystallinity of the substrate and this seeding method makes possible the growth of vertically oriented ZnO nanowires on various types of substrates.

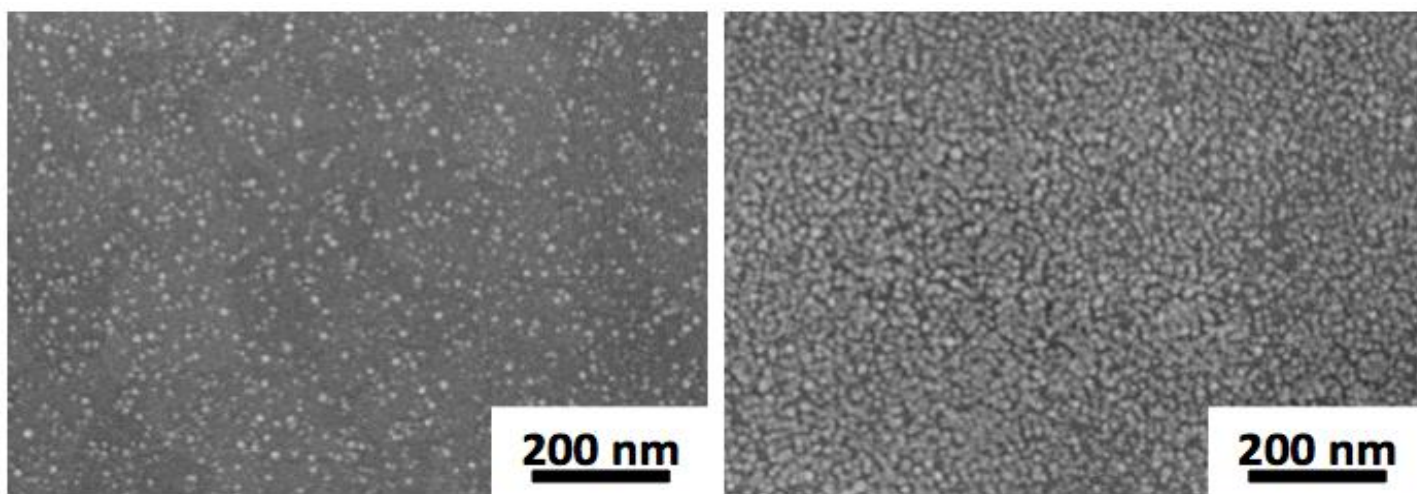
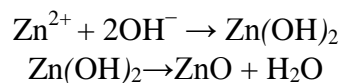
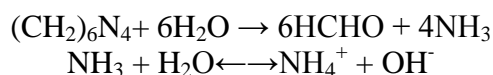


**Figure 1.** SEM images showing the ZnO island seeds. Density of the ZnO island seeds can be increased by applying the seeding method more than once.

---



ZnO nanowires can be grown on the seeded substrate by the thermal decomposition of zinc nitrate and hexamethylenetetramine (HMTA) in aqueous solution. Zinc nitrate supplies  $\text{Zn}^{2+}$  ions and HMTA maintains the solution's pH at 7, providing a controlled supply of hydroxide ions according to the following reaction:



At elevated temperatures, the concentration of  $\text{OH}^{-}$  ions and  $\text{Zn}^{2+}$  ions exceed critical values, therefore nucleation and growth of ZnO nanowires begin at the ZnO nanocrystal seeds according to the following reaction:

Critical diffusion of the monomers and subsequent limited growth make it possible to control the diameter of the ZnO nanowires simply by varying the concentration of the precursors while keeping the same 1:1 ratio<sup>9</sup>. Increasing the precursor concentration by one order of magnitude will increase the diameter or thickness of the ZnO nanowires by one order of magnitude. Length of the ZnO nanowires can be varied by increasing the time the nanowires are left in the growth solution. Figure 2 shows the increase of ZnO nanowire length by increasing the growth time from 1.5 hours to 4 hours. The thickness of the ZnO nanowires is not greatly affected by the prolonged growth time due to the growth habit where the *c* axis is the fastest and preferred growing direction.

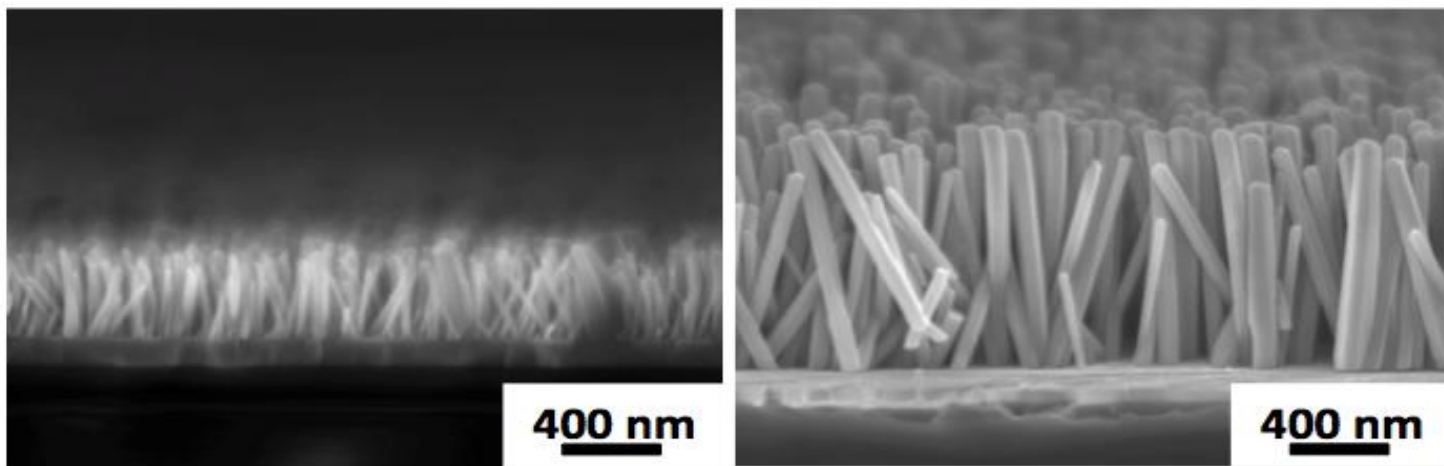


**Figure 2.** SEM images of ZnO nanowires grown by varying the time left in solution. A) ZnO nanowires grown for 1.5 hours. B) ZnO nanowires grown for 4 hours.

The morphology of the ZnO nanowires was characterized using a scanning electron microscopy

(SEM) and x-ray diffractometry (XRD). The vertical orientation of the ZnO nanowire is observed

in the cross sectional SEM image in figure 2 and also by the large intensity (0002) peak, corresponding to the *c* axis, present in the XRD spectrum in figure 3. The optical properties of ZnO nanowires were characterized by ultraviolet-visible spectroscopy (UV-Vis) and photoluminescence

spectroscopy (PL). The absorption edge at ~370 nm present in the UV-Vis spectrum, and the high intensity peak ~370 nm on the PL spectrum correspond to the large band-gap of ZnO. The broad peak ~600 nm present in the PL spectrum corresponds to oxygen and zinc vacancy defects.

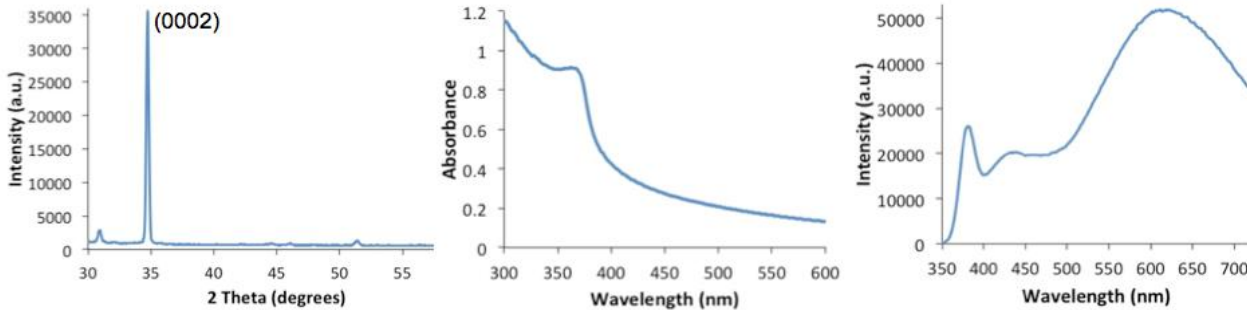


**Figure 3.** Characterization of the vertically oriented ZnO nanowires. A) X-Ray Diffractometry spectrum. B) Ultraviolet-Visible spectrum. C) Photoluminescence spectrum.

Cadmium doping of the ZnO nanowires was achieved by the substitution of 30% molar weight Zinc Nitrate precursor with Cadmium Nitrate precursor in the growth solution and varying the temperature of the reaction. There was no change observed in the morphology of cadmium doped ZnO nanowires as shown by figure 4, indicating that cadmium atoms were incorporated into the ZnO structure without any significant structure change. The optical absorption characteristics of the cadmium doped ZnO nanowires were measured with a UV-Vis spectrometer and a slight redshift of the band-gap absorption edge was observed. It was found that the redshift increased linearly with growth solution temperature as shown by figure 5, and further temperature increase was not possible because boiling of the growth solution was observed. The cadmium doped ZnO nanowires were further characterized by scanning electron microscope equipped with energy dispersive x-ray spectroscopy (EDX), which showed weak, but non-

zero, cadmium signals. The combined evidence of the redshift as indicated by the UV-Vis analysis and the weak cadmium peaks as indicated by EDX suggest that very low level of doping was accomplished despite the significant amount of substituted cadmium nitrate in the growth solution. One speculation as to why low level of doping is achieved is that the thermodynamically favored reaction at equilibrium at the given conditions is one in which the energetics favor only the incorporation of zinc, and the energy barrier for the incorporation of cadmium is high, so there is very low level of doping. In order to incorporate more cadmium ions into the structure, the deposition process has to be driven further away from equilibrium where only the zinc incorporation is favored. The results presented indicate that increasing the temperature is one way of doing this but it is a very limited technique. This problem is currently being examined in order to achieve significant doping levels.

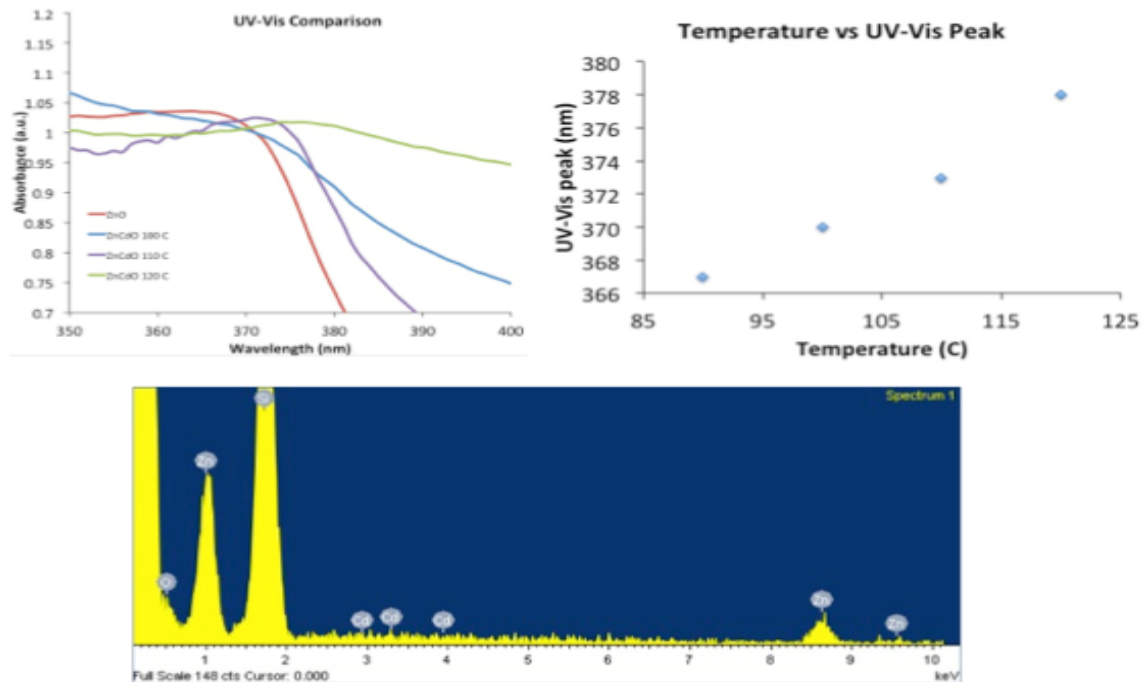


**Figure 5.** A) Normalized UV-Vis analysis of the redshift in the band-gap absorption edge. B) Plot showing redshift peak dependence on growth solution temperature. C) EDX spectrum showing weak cadmium peaks.

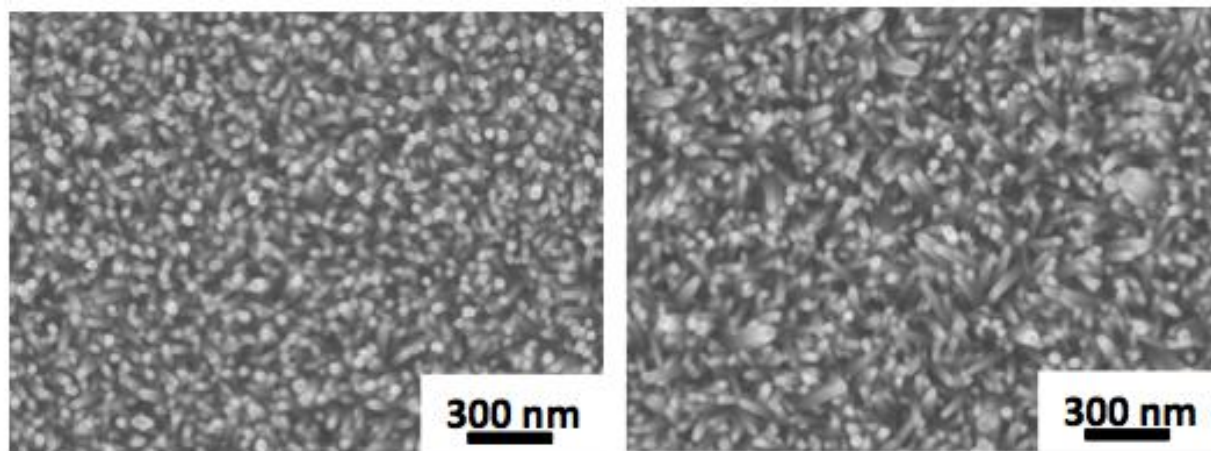


**Figure 4.** Top view SEM images of a) control undoped and b) cadmium doped ZnO nanowires.

The device efficiency of organic photovoltaic devices is often limited by poor charge collection and transport, and high rate of recombination. Vertically oriented ZnO nanowire arrays can be

used to effectively collect and transport electrons created within the bulk heterojunction of organic photovoltaics. ZnO nanowires have high electron mobility and provide a direct path to an electrical

contact, greatly improving charge collection in these devices. Preliminary feasibility tests based on an inverted photovoltaic devices with a heterojunction active layer consisting of poly(3-hexylthiophene) (P3HT) and [6,6]-phenyl C61-butyric acid methylester (PCBM) polymers confirmed that ZnO nanowire charge collectors could improve device efficiency by ~67%. The

device structure of the photovoltaic devices is shown in figure 6 and the current-voltage characteristics are shown in figure 7. It should be noted that the short circuit current and open circuit voltage remained nearly constant in both devices, but the fill factor significantly increased, indicated better charge collection due to ZnO nanowires.

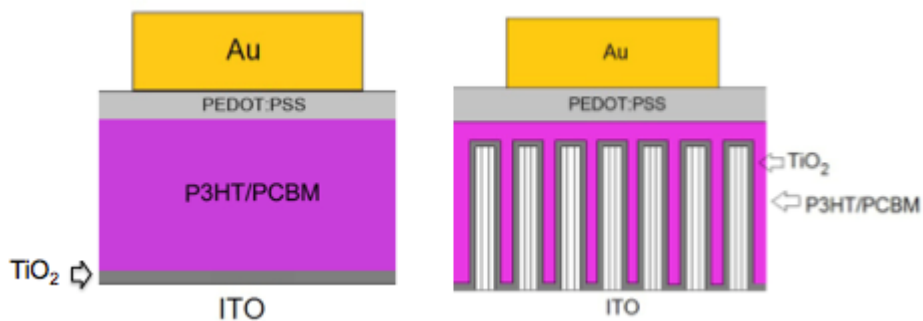
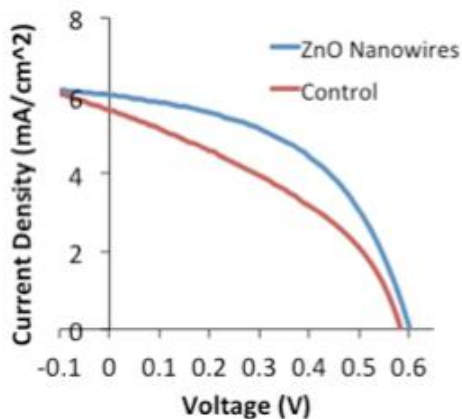


**Figure 6.** Device structures of A) planar contact inverted photovoltaic device and B) ZnO nanowire contact inverted photovoltaic device.



	Number of Samples	Mean Efficiency (%)	Mean Voc (V)	Mean Jsc (mA/cm <sup>2</sup> )	Mean FF
Control	5	1.24 ± 0.01	0.58 ± 0.001	5.6 ± 0.06	0.38
ZnO Device	5	1.67 ± 0.01	0.60 ± 0.001	5.7 ± 0.06	0.50

**Figure 7.** A) Current-voltage characteristics showing the increase in fill factor. B) summary of the photovoltaic device measurement parameters.

### Conclusion.

ZnO nanowires were grown and characterized by SEM, UV-Vis spectroscopy, photoluminescence

spectroscopy, and x-ray diffractometry. Nanowire morphology was examined by varying the growth parameters and it was found that the length of the

nanowires is dependent on the time left in growth solution while the width of the nanowires is dependent on the precursor concentration. Low-level doping of ZnO nanowires with cadmium atoms was achieved by substituting the zinc nitrate precursor with cadmium nitrate. The doped nanowires were characterized by SEM, UV-Vis spectroscopy and energy dispersive x-ray spectroscopy. The dependence of reaction temperature on the level of cadmium doping was examined and found to have a linear trend. ZnO nanowires were used as charge collectors in inverted organic photovoltaic devices and it was shown that device efficiency increased by ~67% mainly through the increase in fill factor due to more effective charge collection.

#### **Acknowledgements**

Department of Energy, Brookhaven National Laboratory, Dr. Charles T. Black

#### **References**

1. N. Saito, H. Haneda, T. Sekiguchi, N. Ohashi, I. Sakaguchi, K. Koumoto, *Adv. Mater.* 2002, **14**, 418.
2. J.Y. Lee, Y.S. Choi, J.H. Kim, M.O. Park, S. Im, *Thin Solid Films* 2002, **403**, 533.
3. N.W. Emanetoglu, C. Gorla, Y. Liu, S. Liang, Y. Lu, *Mater. Sci. Semicond. Process.* 1999, **2**, 247.
4. Lehman, H. W.; Widmer, R. *J. Appl. Phys.* 1973, **44**, 3868.
5. Agarwal, G.; Speyer, R. F. *J. Electrochem. Soc.* 1998, **145** (8), 2920-2925.
6. K. Keis, E. Magnusson, H. Lindstrom, S.E. Lindquist, A. Hagfeldt, *Sol. Energy* 2002, **73**, 51.
7. G. Chu, Z. Xiong, S. Zhao, *J. NANosci. Nanotechnol.* 2010, **10** (8), 4893-4896
8. L. Vayssieres, A. Hagfeldt, S.-E. Lindquist, *Pure Appl. Chem.* 2000, **72**, 47.
9. L. Vayssieres, *Advanced Materials*, 2003, **15**, 464-466.

# Molecular Dynamics Simulation of Dissociation Kinetics and Vibrational Energy Distribution

Rui Lin Tan

Department of Material Science and Engineering, *Chemical and Molecular Engineering Program*,  
Stony Brook University, 11794, NY, USA

---

## Abstract

The goal of the simulation was to model the atomic and molecular interactions of simple diatomic molecules like hydrogen and oxygen. The Morse potential is used to perform the atomic interaction calculation since only vibrational interactions are possible for diatomic molecules. Interactions outside the molecule are modeled using the Lennard-Jones potential because it is one of the easiest an accurate potential correlation can be used in simulations. The vibrational energy level distribution of this model demonstrated excellent agreement with the Boltzmann distribution. In this molecular dynamics simulation, dissociation occurs when the atomic potential energy (Morse potential energy) between two vibrating atoms exceeds a critical value, which related to the bond dissociation energy. Recombination is modeled as the reverse process of dissociation. This modeling method enables a system to start in a state of molecules orderly aligned proceed to an equilibrated state in which molecular potential energy is minimized. The molecular dynamics simulation accurately modeled both the rate of dissociation and the ratio of species at equilibrium.

*Keywords:* Boltzmann distribution; degree of dissociation; Verlet algorithm; Lennard-Jones potential; Morse potential

---

## Introduction

Computer simulations act as a bridge between microscopic length and time scales and the macroscopic world of the laboratory. It is beneficial to do process simulations before the process is taken place in real-world setting especially if the process is very expensive. Molecular dynamics simulation is one of the popular simulation techniques in which a small atomic-scale system is simulated using basic physics law to obtain real-world properties. The vibrational energy distribution and the degree of dissociation within a system of hydrogen and oxygen molecules was modeled using molecular dynamics (MD).

In general molecular systems consist of a large number of particles. It is practically impossible to find the properties of such complex systems analytically by solving equations of physics. MD simulation circumvents this problem by simplifying the molecular system into pair

interactions and use simple force field<sup>1</sup>. This computational method calculates the time dependent behavior of a molecular system. MD simulations can be used to investigate the structure, dynamics and thermodynamics of molecular systems and their complexes.

In order to demonstrating the power of the MD simulation technique, a simple chemical reaction, namely combustion of hydrogen gas in oxygen, is studied. The first step in simulating a reacting gas by molecular dynamics is determining how vibrational energy is distributed among the atoms. The harmonic and anharmonic vibration distribution will be compare to the theoretical Boltzmann distribution<sup>2</sup>. Once this is accomplished, modeling simple reactions is possible. Chemical reaction in this simulation is only considered to have only simple dissociation and recombination mechanisms.

## Molecular Dynamics Algorithm

In molecular dynamics, the most commonly used time integration algorithm is probably the so-called Verlet algorithm. The advantage of this algorithm is it is relatively easy to program and provide good stability for a relatively large time step. This is significant because it can save a lot of computation time by using larger time step, in the order of picoseconds rather than in the order of femtoseconds.

To use this algorithm, first, the position is advanced one time step and the velocity is advanced half of a time step, as shown in the following equations:

$$r(t + \Delta t) = r(t) + v(t)\Delta t + \frac{\Delta t^2}{2} a(t) \quad (\text{eqn 1})$$

$$v\left(t + \frac{\Delta t}{2}\right) = v(t) + \frac{\Delta t}{2} a(t) \quad (\text{eqn 2})$$

The  $r(t)$  represents the position function,  $v(t)$  is the velocity function and  $a(t)$  is acceleration function.

$\Delta t$  is the time step. At this point, the forces, but intermolecular and intramolecular, are computed and velocity is advanced another half time step.

$$v(t + \Delta t) = v\left(t + \frac{\Delta t}{2}\right) + \frac{\Delta t}{2} a\left(t + \frac{\Delta t}{2}\right) \quad (\text{eqn 3})$$

Experimental results show that the Verlet algorithm accurate to the order of  $(\Delta t)^3$ . This level of accuracy is sufficient for the simulation described in this paper<sup>3</sup>.

For simplicity, the entire simulation is done in two dimensional. As a result of that, much of the molecular collisions are omitted and thus some problem is created. During the advancement of molecules, a thermostat is necessary to prevent a molecule to have excessively large kinetic energy by scaling it down to match the expected thermal distribution of energy. A thermostat is therefore

necessary for the molecular system to reach equilibrium.

The overall algorithm can be more easily understood by summarizing it into the following diagram.

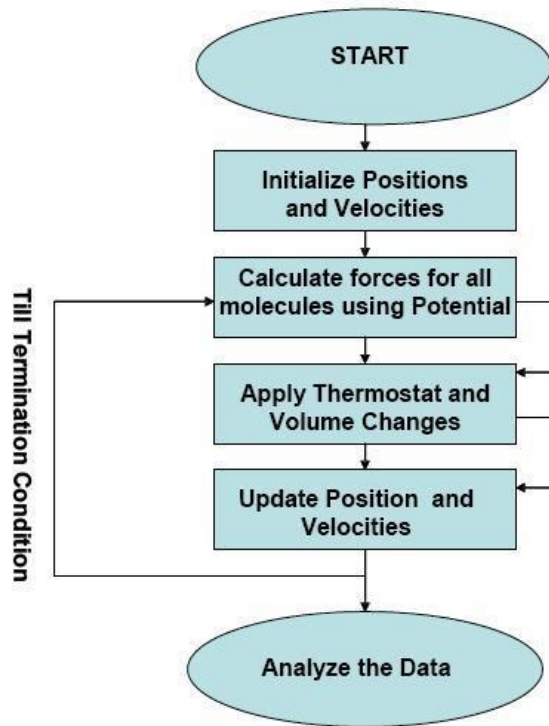


Figure 1. Flow chart diagram explaining the Verlet algorithm.

## Intermolecular Potential and Forces

In molecular dynamics, the potential is taken to be pairwise additive. This means that the total energy in the system is a sum of the isolated two-body contributions. Three body and higher terms are usually neglected because of the vast increase in computational time and their relatively small influence on gaseous systems. The most commonly used pairwise additive potential,  $u$ , for modeling intermolecular forces between atoms separated by a distance  $r$  is the one proposed by Lennard-Jones<sup>4</sup>.

$$u(r_{ij}) = 4\epsilon \left[ \left( \frac{\sigma}{r_{ij}} \right)^{12} - \left( \frac{\sigma}{r_{ij}} \right)^6 \right] \quad (\text{eqn 4})$$

The other parameters used in this equation such as  $\sigma$  is the Lennard-Jones size parameter and  $\epsilon$  is the Lennard-Jones energy parameter. For hydrogen molecules simulated,  $\sigma = 0.27$  nm and  $\epsilon = 0.0025$  eV. For oxygen molecules simulated,  $\sigma = 0.30$  nm and  $\epsilon = 0.0056$  eV.

Since the intermolecular forces are necessarily conservative, the force resulting from the above potential is the negative of the derivative of the potential function with respect to the molecular separation distance,  $r_{ij}$ .

$$f(r) = -\frac{du(r)}{dr} = 24 \frac{\epsilon}{\sigma} \left[ 2 \left( \frac{\sigma}{r} \right)^{13} - \left( \frac{\sigma}{r} \right)^7 \right] \quad (\text{eqn 5})$$

### Intramolecular Potential

The potential between two atoms of the same molecule differs slightly from the intermolecular potential. In order to conform to spectroscopic experiments, the intramolecular

potential is required to have a potential well at the mean bond length and approach the dissociation energy as the atoms become infinitely separated<sup>5</sup>. Also, like the Lennard-Jones potential, it must go to infinity as the atoms approach each other. One such model that conforms to these specifications is the Morse potential. This potential is given by

$$V(r) = D_e (1 - e^{-a(r-r_e)})^2 \quad (\text{eqn 6})$$

$D_e$  is the spectroscopic energy,  $r$  is the distance between two atoms.  $r_e$  is equilibrium bond length.  $a$  is the vibrational parameter which can be calculated using spectroscopic data

$$a = 2\pi c \omega_e \sqrt{\frac{\mu}{2D_e}} \quad (\text{eqn 7})$$

In this equation,  $c$  is the speed of light,  $\mu$  is reduced mass of atom and  $\omega_e$  is the spacing of vibrational energy levels<sup>6</sup>.

Compared to long range potential like Lennard-Jones potential, the Morse potential permits smaller separation distances between the atoms. This comparison is best illustrated by the following graphs showing both potential function of the same set of axes.

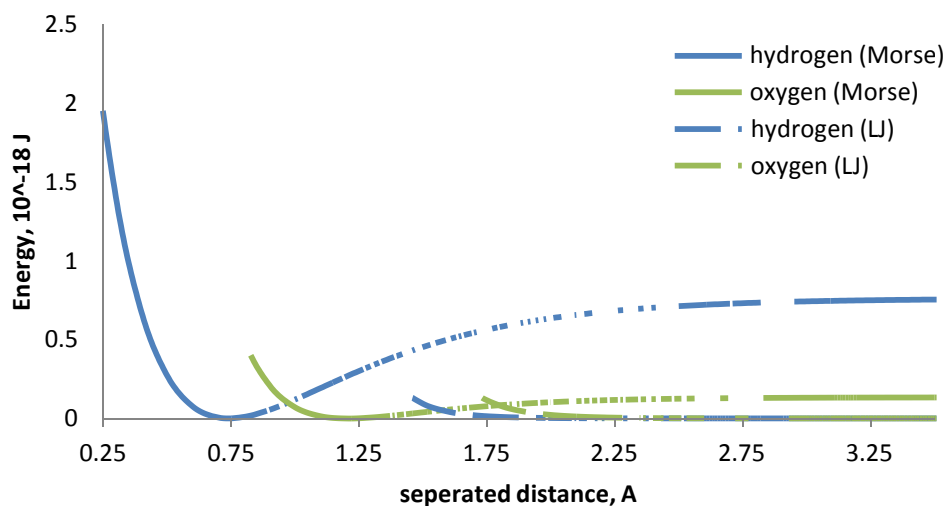


Figure 2. Comparison between Lennard – Jones (intermolecular) and Morse potential (intramolecular) functions with respect to separated distance.

## Vibrational Energy Distribution

The first goal of this molecular dynamics simulation was to model the vibrational energy distribution within a system of oxygen molecules and a system of hydrogen molecules. Vibrational energy is expected to be distributed in discrete energy levels according to the Boltzmann distribution. The normalized fraction of molecules,  $N^*/N$ , with respect to a specific energy level,  $v$ , can be calculated using the following equation.

$$\frac{N^*}{N} = \frac{g_i e^{-\epsilon_v/kT}}{\sum g_i e^{-\epsilon_v/kT}} \quad (\text{eqn 8})$$

In this equation,  $g_i$  is the degeneracy,  $\epsilon_v$  is the vibrational energy,  $k$  is the Boltzmann constant and  $T$  is temperature. For vibrational energy distribution, there is no degeneracy. This means that there is only one state per level or  $g_i$  is unity.

However, since vibrational energy increases in discrete increments, a relationship must be formed between the quantum energy levels and the vibrational energy. This relationship is given by the following correlation.

$$\epsilon_v = \omega_e(v + .5) - x_e \omega_e (v + .5)^2 - .5\omega_e + .25x_e \omega_e \quad (\text{eqn 9})$$

The parameter  $n$  is the quantum energy level,  $\omega_e$  the spacing of the vibrational energy levels, and  $x_e \omega_e$  is the first anharmonic correction.

The molecular dynamics code used in this simulation will output vibrational energy. It then must be converted to discrete quantum levels by solving for  $n$ . One simple to do this is acknowledging the above equation is a quadratic equation. Simply using the quadratic formula, the smaller root is the vibrational energy level. This operation is performed on every molecule at every time step. One further complication is that  $n$  must be an integer. The most efficient method to

convert  $n$  is simply to truncate it. Truncation ensures that the zero energy level bin is equal in size to the other bins. The last step is to count the number of molecules in each energy level.

## Results and Discussion

One of the disadvantages of molecular dynamics simulation is the time required for complete is proportional to the square of the number of molecule simulated when using brute force method to calculate all interactions. The number of molecules simulated was 350 in a box with periodic boundary conditions. A time step of 0.0001 nanoseconds was chosen in order to obtain high resolution data in order to have a better understanding of events like a chemical reaction that happen in a nanosecond time scale, which impossible to observe in laboratory experiments.

Besides choosing a suitable simulation method, the parameter used in this simulation is just as important. These parameters are summarized below<sup>7</sup>.

Table 1. Important parameters used in molecular dynamics simulation.

	Hydrogen	Oxygen
$\sigma$ (eV)	0.27	0.30
$\epsilon$ (nm)	0.0025	0.0056
$D_e$ (J)	$7.60 \times 10^{-19}$	$8.36 \times 10^{-19}$
$r_e$ (Å)	0.74144	1.21
$\beta$ (Å <sup>-1</sup> )	1.94476	2.65
$\omega_e$ (cm <sup>-1</sup> )	4401.21	121.33
$\chi_e \omega_e$ (cm <sup>-1</sup> )	1580.19	11.99
Boltzmann constant (cm <sup>-1</sup> /K)	0.69503476	

For simulating interactions of two different molecules, the weight average of the Lennar-Jones parameters is used.

Figures 3 and 4 below are the calculated distribution of vibrational energy of both hydrogen and oxygen comparing to Boltzmann distribution at a temperature of 6100 K. The simulation results,

shown as triangle markers closely match the calculation results. In other words, the vibrational properties of the molecule have successfully simulated.

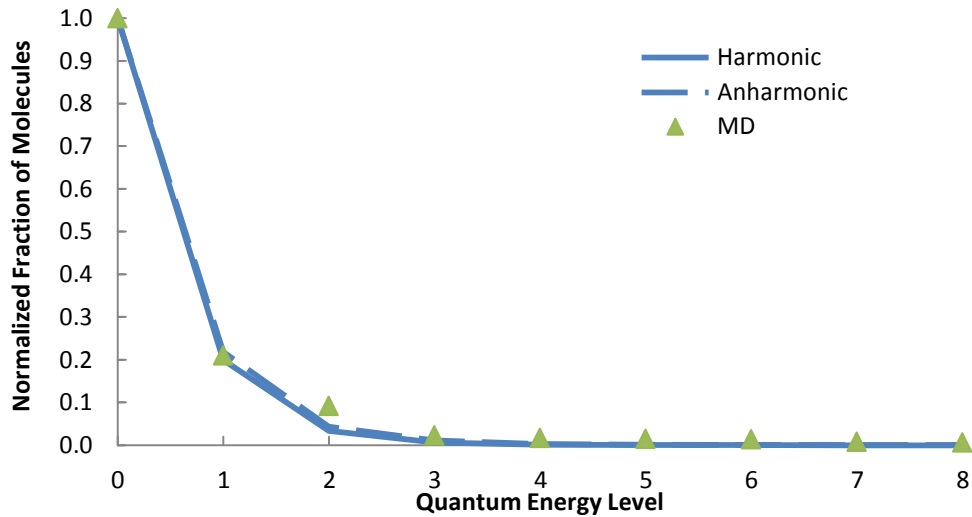


Figure 3. Vibrational energy distribution of hydrogen molecules comparing to theoretical values.

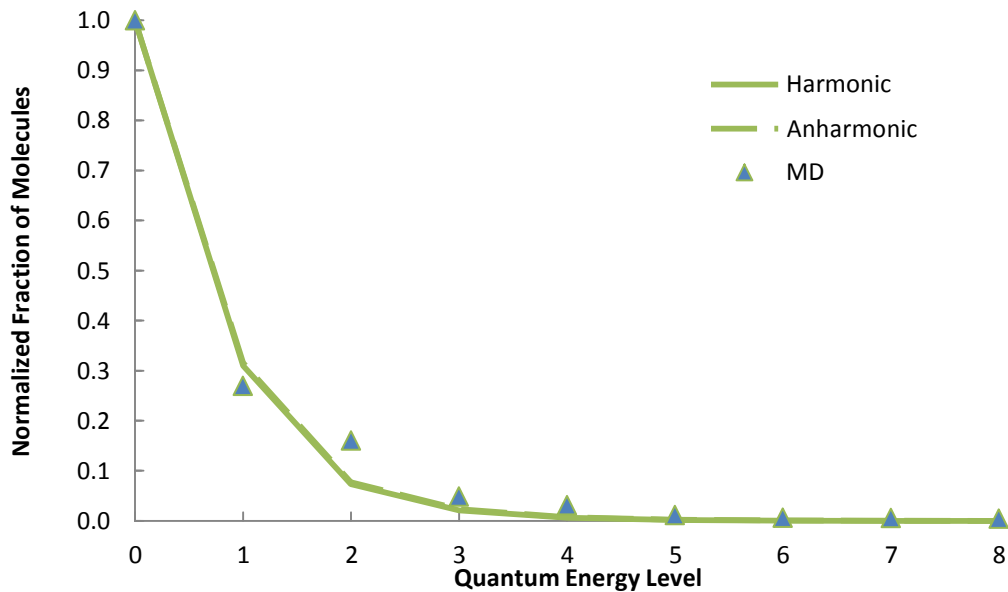


Figure 4. Vibrational energy distribution of oxygen molecules comparing to theoretical values.

Once the correct vibrational energy distribution is established, the simulation of chemical reaction can begin. The percent of dissociation of

both hydrogen and oxygen molecule is illustrated in figure 5 below.

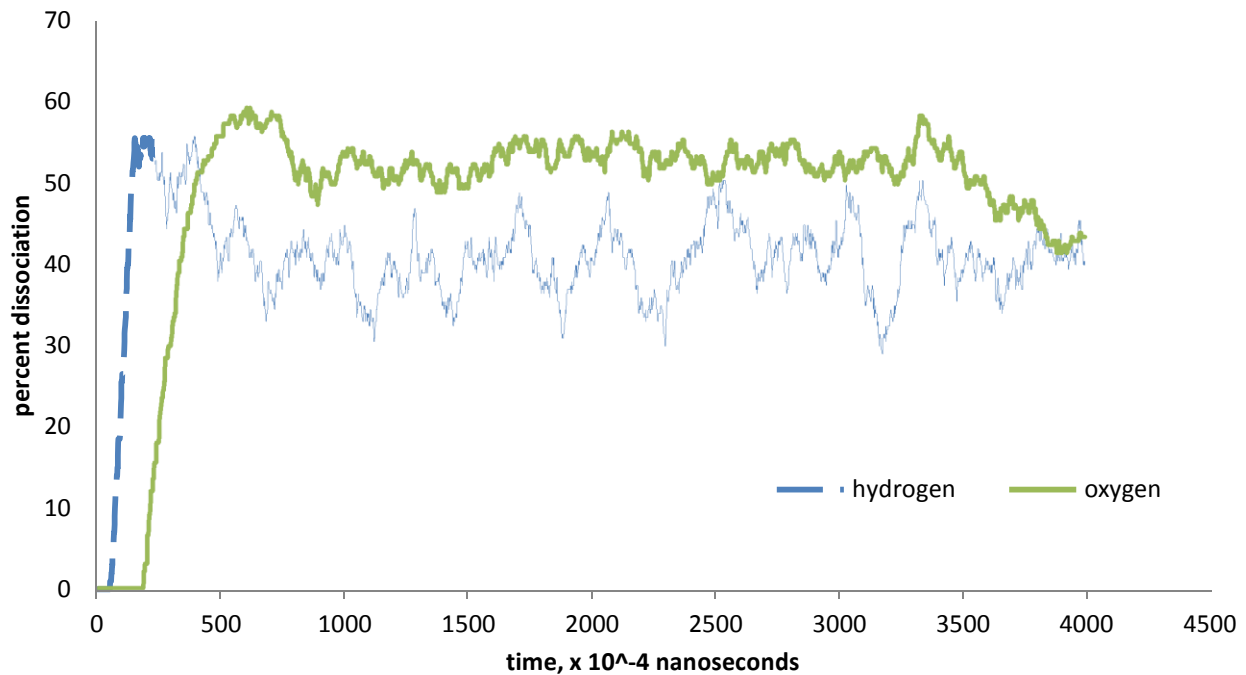


Figure 5. Percent dissociation of hydrogen (blue) and oxygen (green) in simulation.

Figure 5 above shows that the dissociation of both hydrogen and oxygen molecules happen within 0.050 nanoseconds. This is comparable to literature values. The average percent of dissociation of hydrogen is 39.94%. The average percent of dissociation of oxygen is 51.05%. The reaction takes place in an average temperature of 6100 K. Literature values of this kind of simulation show that the percent dissociation of hydrogen fluctuates between 35% and 40%. The percent dissociation of oxygen fluctuates between 45% and 50%. The simulation result did not match the expected values, although not closely.

From figure 6 (shown below), temperature fluctuation during the simulation can be as large as 1000 K. This huge fluctuation is expected because a simple thermostat, called Langevin thermostat was

chosen for 2D rather than a 3D simulation in order to keep calculation simple. Unlike 3D molecular dynamics simulations, a robust thermostat is crucial to 2D simulations. A thermostat functions as a heat bath to absorb excessive thermal energy in order to maintain thermal equilibrium. For reference the performance of Langevin thermostat is compared to two other popular thermostats, namely velocity scaling thermostat and Nose-Hoover thermostat.

The Nose-Hoover thermostat has the best performance of the three. If it is chosen to be the thermostat used in the simulation, the fluctuation of temperature should be smaller.

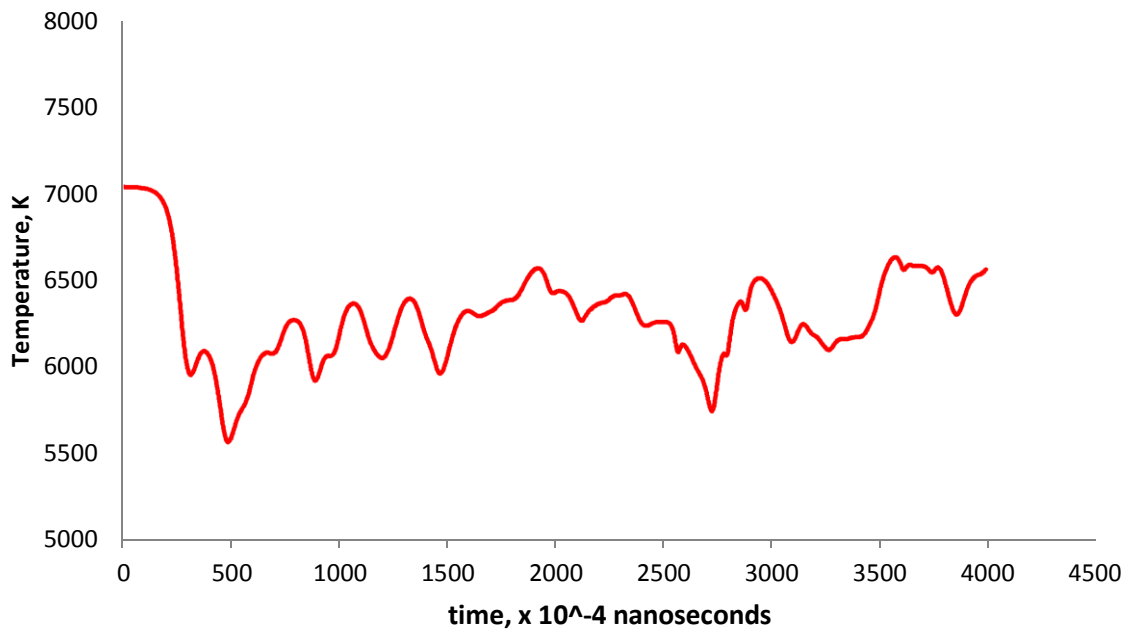


Figure 6. Temperature fluctuation during simulation.

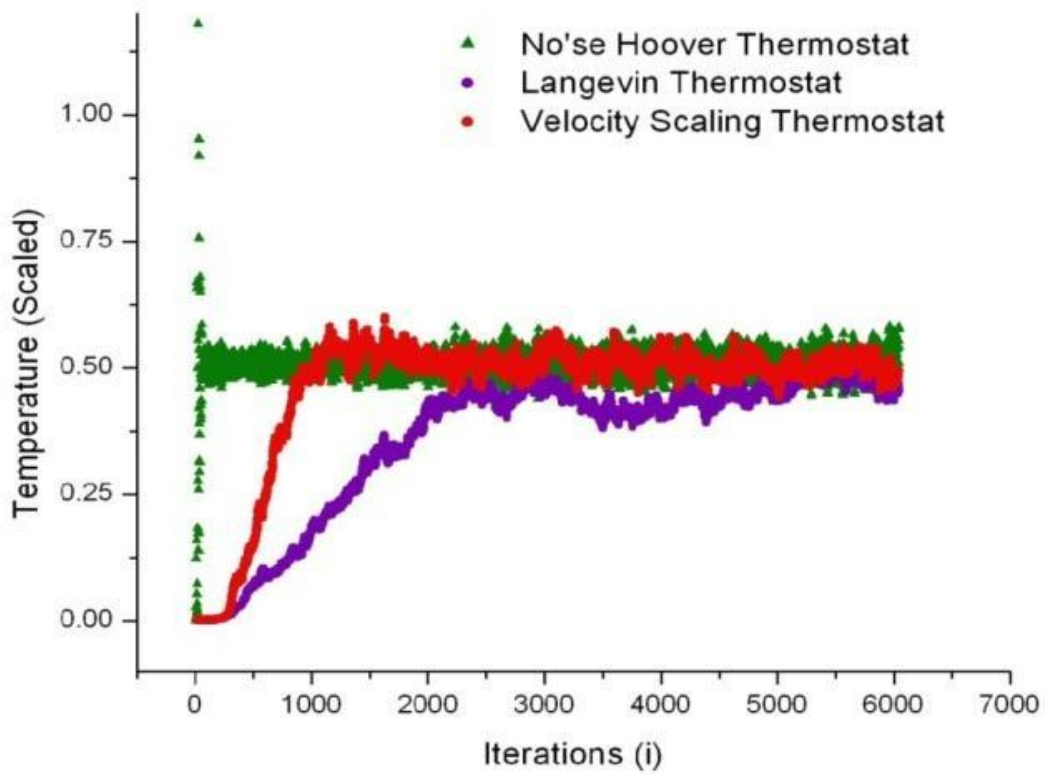


Figure 7. Comparison of thermostat performances.

## Conclusion

During the simulation, when two molecules collide with each other with sufficient momentum, the bond between the atoms of each molecule will be contracted or expanded according to the total Lennard-Jones force at that instant. Both the molecular vibration calculation and degree of dissociation calculation are based on this simple atomic motion. Other types of atomic motion like bond rotation and sigma bond pi bond breaking are omitted.

Results of the vibrational energy distribution calculations have shown acceptable agreement with the Boltzmann distribution. Both the rate of dissociation and the equilibrium degree of dissociation have also compared well to kinetic theory. This investigation has demonstrated that simple large-scale chemical reactions can be modeled by molecular dynamics.

Although the simulation results in this simulation generally agree with literature values, however, it can be improved. In the future, a Verlet neighbor list algorithm can be incorporated into the molecular dynamics code to significantly shorten the computation time for simulating larger number of molecule. Having a larger amount of molecule in the simulation should provide better and more accurate results. Furthermore, for the sake of realism, a more complicated force field which includes bond rotation and can be used.

Being able to simulate gas reaction using molecular dynamics is important for the development of future rocket propulsion systems. In such systems, reactions usually carry out in extremely high pressure environment. This makes laboratory scale experiment very difficult. In cases like this, molecular dynamics simulation becomes very useful. Sometimes a computer simulation is probably the only way to study such reaction in great detail.

## References

1. Peter Signell. *“Diatomic Molecules: Properties From Rotation – Vibration Spectra.”* 2007.
2. Michael P. Allen. *“Introduction to Molecular Dynamics Simulation.”* NIC Series. Vol. **23**, pp. 1-28. 2004.
3. Paul F. Batcho and Tamar Schlick. *“Special stability advantages of position-Verlet over velocity-Verlet in multiple-time step integration.”* Journal of Chemical Physics. Vol. 115, number 9. 2001.
4. G. H. Hudson, J. C. McCoubrey. *“Intermolecular Forces Between Unlike Molecules.”* 1960. Web. 4/29/2012.
5. Theresa Julia Zielinski. *“Exploring the Morse Potential.”* American Chemical Society. 1998.
6. Valerie Wathelet, Benoit Champagne, David H. Mosley, Jea-Marie Andre, Sandro Massidda. *“Vibrational frequencies of diatomic molecules from Car and Parrinello molecular dynamics.”* Chemical Physics Letters. 1997.
7. Daniel D. Konowalow, Joseph O. Hirschfelder. *“Morse Potential Parameters for O-O, N-N and N-O Interactions.”* The Physics of Fluid. Vol 4, No. 5. May, 1961.
8. D. Brown, J. H. R. Clarke. *“A comparison of constant energy, constant temperature and constant pressure ensembles in molecular dynamics simulations of atomic liquids.”* Molecular Physics. 1984.

# Model drug delivery system using gelatin microspheres

<sup>1</sup>Zhenghao Li, <sup>2</sup>Xin He, <sup>1,2</sup>Yizhi Meng

<sup>1</sup>Department of Chemical and Molecular Engineering

<sup>2</sup>Department of Materials Science and Engineering

Stony Brook University, Stony Brook, NY, 11794-2275, USA

---

## Abstract

Gelatin is naturally-derived material. Because of its great biocompatibility, biodegradability and non-toxicity, gelatin microspheres could become the more preferred drug delivery vehicles. We developed a fabrication method in which mineral oil and acetone were replaced by olive oil and Bio-Solv (a commercial acetone replacement solvent that is 100% biodegradable and non-toxic). To fabricate the microspheres, a homogeneous gelatin solution was first prepared in water. Then, based on the water in oil emulsion, the aqueous gelatin phase was added drop by drop into the olive oil phase with constant stirring in the ice bath. Microspheres in the oil phase were further crosslinked with EDC/NHS solution and stirred to form the final gelatin microspheres. By comparing the microspheres at different fabrication conditions such as stirring speeds and durations, the stabilities, shapes and sizes of microspheres were characterized with an optical microscope. It was concluded that by increasing the stirring speed and stirring period, the size of microspheres decreased.

Keywords: Gelatin; Water in Oil emulsion; microspheres; shear force; stability

---

## 1. Introduction

In the drug delivery system, conventional oral dosage forms do not provide a sustained drug release rate. In addition, its burst effect may have potential side effects such as the toxicity from the overdose. Currently, researchers have developed a unique method for drug delivery, which is the microsphere. It can be made with controllable drug release rates, which provide an effective supply to the target cells [1]. However, many microsphere drug delivery systems involve the use of synthetic polymers and organic solvents, where toxicity is a potential risk to tissues. For example, the fabrication process of PLGA microspheres involved the use of toxic organic solvents. In addition, the

degradation of PLGA was determined to create an acidic environment. Because of this decreasing pH value, it could cause potential inflammatory response [2]. Later on, researchers has started to use natural materials in fabricating the microspheres. In Jun Wang's study, material like calcium carbonate/Carboxymethyl chitosan has been used to fabricate microspheres and nanospheres. The drug release profile was shown to be effectively sustained [3]. Similarly, according to Fu Yin Hsu's study, material like hydroxyapatite and collagen has been used to fabricate microspheres. It was tested that osteoblast cells could adhere on to microspheres, which could be used in treating the bone defect in future [4]. However, a more preferable green process in

fabricating the microspheres is still needed. Gelatin is a natural product that is derived from collagen, which is the main component of extracellular matrix of bone. Due to its great biocompatibility, biodegradability and non-toxicity, there will be no side effects such as significant pH change when it degrades [5]. Besides gelatin, common mineral oil and acetone are being replaced by cooking material olive oil and Bio-Solv (a commercial acetone replacement solvent that is 100 % biodegradable and non-toxic). With those green and cheap materials, we developed feasible water in oil emulsion process in manufacturing the gelatin microspheres.

Briefly, gelatin solution is prepared and then added to olive oil phase, which contains Span 85 emulsifier, drop by drop with constant stirring in ice bath. After a certain period of time, EDC/NHS (1-ethyl-3-(3-dimethylaminopropyl) carbodiimide)/N-hydroxysuccinimide) is added in order to crosslink the gelatin beads. By performing gravity filtration, gelatin beads are collected and washed with Bio-Solv in removing the excess oil. Final gelatin microspheres are characterized with optical microscope. Size distribution are recorded and analyzed based on stirring speed and time.

## 2. Materials and Methods

### 2.1. Materials:

Porcine gelatin (Great Lakes, unflavored gelatin, 16oz) and olive oil (Filippo Berio, extra light tasting, 101.4Fl oz) were purchased from supermarket. Span 85 was purchased from Sigma-Aldrich. EDC and NHS were also purchased from Sigma-Aldrich. Bio-Solv was purchased from MAS products (Phoenix Resins, Inc. company, USA). Acetone was from Dr. Yizhi Meng's lab. Equipment like Hot plate stirrer (The Lab Depot Inc.), pH meter (HANNA pH

213 microprocessor pH meter) and optical microscope were from Dr. Yizhi Meng's lab.

### 2.2 Preparation of gelatin microspheres

The method was designed based on Habraken's gelatin microsphere preparation method [5]. A homogeneous gelatin aqueous phase solution was first prepared by adding 1g of gelatin into 10ml DI water with constant stirring and heating at 60°C. Then 50ml olive oil with 2% w/w Span 85 oil phase was prepared and stirred for 5mins. Gelatin solution was added drop by drop into olive oil phase in an ice bath with constant stirring speed and time. The stirring speed and time were adjusted as shown in table 1 and 2. By adding 5ml of (34mM: 17mM) crosslink EDC: NHS solution into the mixture solution, the emulsion process was further stirred for another 1hr under constant stirring in ice bath. Finally, gravity filtration was performed in collecting the particles. Bio-Solv or acetone was used in washing away the excess oil from microspheres.

Stirring speed	Time (before crosslink/ after crosslink)	Description
3 (120rpm)	30min/1hr	Acetone washed
5 (260rpm)	30min/1hr	Acetone washed
7 (600rpm)	30min/1hr	Acetone washed

Table 1. Microspheres fabricated under different stirring speed

Stirring speed	Time (before crosslink/ after crosslink)	Description
5 (260rpm)	10min/1hr	Bio-solv washed
5 (260rpm)	15min/1hr	Bio-solv washed
5 (260rpm)	20min/1hr	Bio-solv washed

5 (260rpm)	25min/1hr	Bio-solv washed
5 (260rpm)	30min/1hr	Bio-solv washed

Table 2. Microspheres fabricated under different stirring time

### 2.3. Characterization of gelatin microspheres

A small amount of gelatin microsphere powder was placed in a 15ml screw cap conical tube. A small portion of 100% ethanol was added into the tube and shaken for 3 minutes. Plastic transfer pipet was used to transfer the dilute gelatin microsphere glass slide. After the evaporation of ethanol, particles were observed on optical microscope and particles' diameters were counted and converted to micrometer size based on the image scale bar.

### 2.4 Correlation of stirring size

Since the stirring speed scale bar on the stirring plate is from 1-9. Referring to the stirring plate's manual and other journal articles, correlation was conducted to convert the stirring scale unit to rpm.

## 3. Results and discussion

### 3.1 Correlation of stirring speed

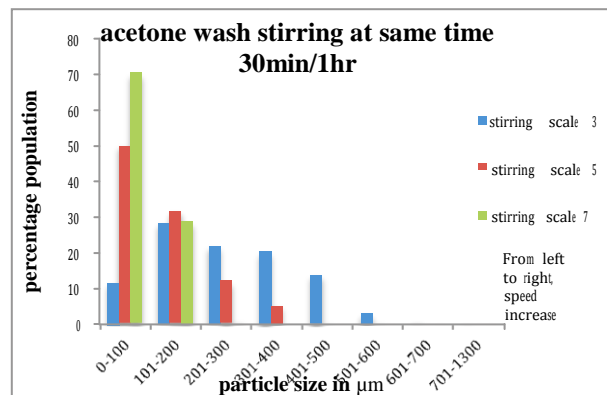


Figure 1. Gelatin microspheres fabricated under different stirring speed

Stirring speed scale	Average size of particles in μm
3 (120rpm)	260
5 (260rpm)	129
7 (600rpm)	82

Table 3. Gelatin microspheres' average size fabricated under different stirring speed but same 30min/1hr stirring period

From figure 1, we see our gelatin particles became smaller and smaller when stirring speed became faster. Referring to Fu's study, collagen microspheres also became smaller when stirring speed increased. Most collagen particles sizes were in the range of 75-150 μm [4]. Comparing the reference with table 3, we see that the stirring scale 5, 30min/1hr sample's particle average size, 129 μm fall in the range of 75-150 μm. Due to the similar physical and chemical properties of collagen and gelatin, I would correlate the stirring scale 5 on our hot plate to be around 200rpm. In addition, referring to manufacture information of Hot plate stirrer from The Lab Depot Inc. It shows that speed range is from 60-1500rpm [6]. The stirring range labeled on the hot plate stirrer is from 1 to 9. Thus, I defined the stirring scale 1 as minimum 60rpm and stirring scale 9 as maximum 1500rpm. With these three points available, correlation equation was determined by excel as shown in figure 2. Stirring scale 3, 5 and 7 were determined to be 120rpm, 260rpm and 600rpm.

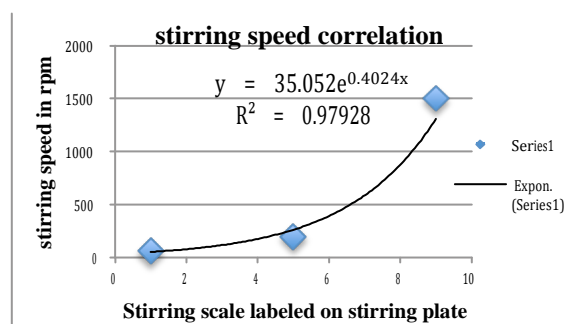


Figure 2. Correlated stirring speed function

3.2. Microsphere morphology and size distribution:

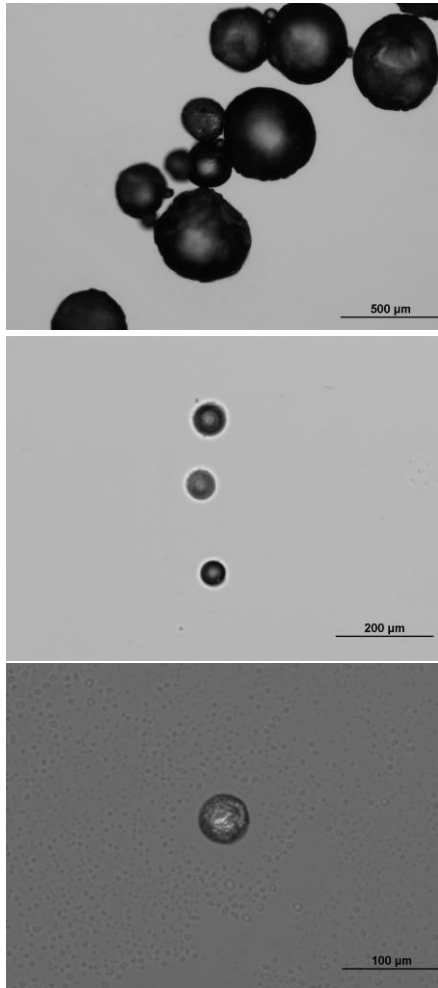


Figure 3. Gelatin microspheres fabricated under 120rpm (top) 260rpm (middle) 600rpm (bottom)

Figure 3 shows the gelatin microspheres prepared in olive oil under constant stirring period 30min/1hr. From figure 3, we concluded the successful fabrication of gelatin microspheres based on the spherical morphology. In addition, by counting the particles sizes, the particle size distribution diagrams were plot and shown below as figure 4 and 5.

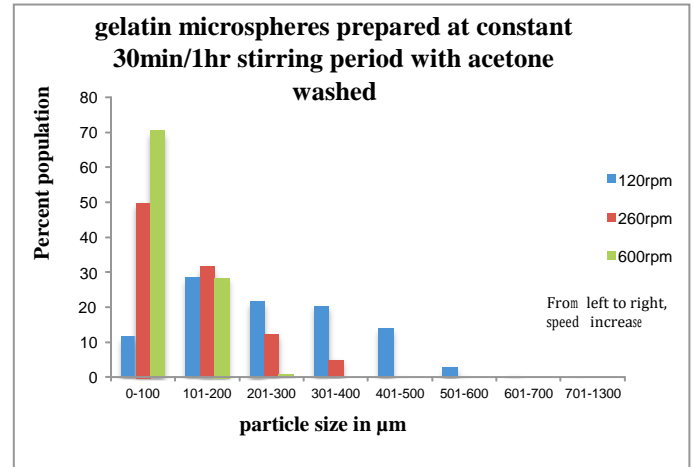


Figure 4. Microsphere's size distribution under different stirring speed but constant stirring period with acetone washed

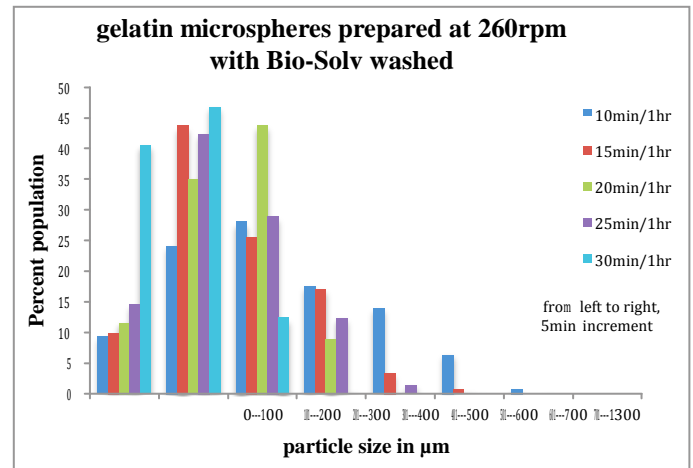


Figure 5. Microsphere's size distribution under different stirring period but constant stirring speed with Bio-Solv washed

Stirring period (before crosslink time/ after crosslink time)	Average microsphere diametersize in µm
10min/1hr	274
15min/1hr	211
20min/1hr	200
25min/1hr	195
30min/1hr	123

Table 4. Microspheres average size fabricated under different stirring period but same stirring speed 260rpm

From figure 4, the only size-determining factor was proposed to be the stirring speed, which were conducted at 120rpm, 260rpm and 600rpm. All microspheres were washed with acetone to remove the excess oil. We can see that under slow stirring speed 120rpm, microspheres had broad size ranges from 0-1300 $\mu$ m. As stirring speed increased, I observed that microspheres size range became smaller and smaller. When stirring speed was adjusted to 600rpm, most particles were in range of 0-200 $\mu$ m. This agrees with table 3 data, where particle's average size decreases with increasing stirring speed. This could be explained based on the rate of coalescence and shear stress. When low stirring speed was used, low shear stress acted on the microspheres. The rate of coalescence could be higher than the rate of breakup of big droplets in the system. Thus, particles were not very stable and results a broad size range of microspheres.

Similarly, figure 5 showed the microspheres fabricated under constant stirring speed 260rpm. The only size-determining factor was proposed to be the stirring period, which was conducted at 10min/1hr, 15min/1hr, 20min/1hr, 25min/1hr and 30min/1hr. All microspheres were washed with Bio-Solv to remove the excess oil. We can see when stirring period was 10min/1hr microspheres had broad size ranges from 0-700  $\mu$ m. As longer stirring period was conducted, microspheres' size range shrink into a smaller range as expected. And it agreed with the table 4 data, where particle's average size decreases with increasing period. As we can see, under 30min/1hr stirring period, most particles range from 0-300  $\mu$ m. When less stirring period was used, particles were not able to well experience the shear force. The rate of coalescence and the rate of breakup of droplets could not reach an equilibrium,

which unstable particles formed with broad size range.

Washing agent	Average microsphere size in $\mu$ m
Bio-Solv	123
Acetone	129

Table 5. Microspheres prepared at constant stirring speed 260rpm and 30min/1hr stirring period with Bio-Solv and acetone washed

From table 5, we can see that either using Bio-Solv or acetone to wash the gelatin microspheres did not significantly affect the particle size. Thus, since Bio-Solv is a biodegradable solvent with limited toxicity when comparing to acetone, Bio-Solv could become a substitute of acetone in washing away the excess oil.

Based on the known stirring speed and average microsphere diameter size, a fluid mechanics correlation for the mean diameter of gelatin microsphere was analyzed and compared to previous studies. As we know, when adding aqueous gelatin solution into olive oil with constant stirring, aqueous droplets were constantly breaking up and coalescence. From previous study, it was found that particles experienced highest shear forces at the edge of the impeller, where particles deformed into smaller particles. On the other hand, the interfacial tension and oil phase' viscosity acted as the restoring forces that tries to maintain the droplet size. Eventually, equilibrium would be established between the rate of break up and the rate of coalescence, where stable particles could be obtained [7]. In addition, the average diameters of microspheres were concluded to be proportional to the weber number, which represents the balance between the inertial shear forces and surface tension forces [7]. It was expressed as equation 1:

$$\frac{d_{avg}}{D} = c * \left( \frac{\rho * N^2 * D^3}{\sigma} \right)^{-3/5} = c * We^{-\alpha} [7]$$

where:

C, constant

$d_{avg}$ , average diameter of microspheres

D, impeller diameter, 0.038m

N, stirring speed in rpm or  $s^{-1}$

$\sigma$ , interfacial tension, 8mN/m

We, weber number

$\rho$ , Olive oil density,  $0.918g/cm^3$

From the previous determined equation 1, a relation between my experimental average particle size and weber number was determined and compared to the previous study. From Foyeke's study, he concluded that with 0.2% w/v of Span 85, the interfacial tension of mineral oil/double distilled water was 8mN/m [8]. In my experiment, olive oil, dilute gelatin solution and 0.2% w/w of Span 85 were used. 0.2% w/w of Span 85 was calculated to be same as 0.2% w/v of Span 85. In addition, since the properties of olive oil and gelatin solution were relatively similar to the mineral oil and distilled water, I would assume the interfacial tension of my system was relatively similar to the mineral oil/double distilled water system. Thus, 8mN/m was defined as interfacial tension of olive oil/gelatin solution with 0.2% w/w of Span 85. With the additional known data such as impeller diameter, olive oil density, stirring speed, the weber number was calculated and listed in table 6.

Stirring speed in rpm	Weber number	Average microsphere diameter in $\mu m$
120	90670	260
260	425647	129
600	2266762	82

Table 6. Weber number determined based on experimentally obtained average microsphere diameter prepared in olive oil at different stirring speed

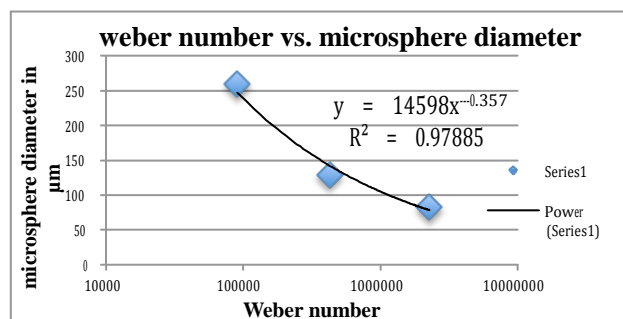


Figure 6. Weber number vs. microsphere diameter

From figure 6, we see that when weber number increase, average particle size decreases. It agreed with the previous study. Since a larger value of weber number indicates a larger ratio of shear forces to surface tension, shear forces were the determining factor in changing the particle size. Thus, by increasing the stirring speed, shear forces increased. As a result, weber number directly increased and particle size decreased inversely. According to the previous studies, the exponent of weber number,  $\alpha$ , has a value of -0.6 [7]. However, it was observed to be a larger value, -0.357 in figure 6. The difference in exponents' value might be caused by the polymer difference since gelatin was the main component of the microspheres in my experiment. In the case of accuracy, further experiments should be conducted to expand the data points in order to fully determine the exponent value.

#### 4. Conclusion

In conclusion, microspheres were successfully fabricated based on the green process. From the experimental data, microspheres were observed to be smaller when the stirring speed and stirring time increase, which due to the effect of shear forces. Most importantly, it was experimentally approved that Bio-Solv, a 100% biodegradable commercial solvent, could become a substitute of acetone, a toxic organic solvent.

## Reference:

1. S. Freiberg, X. X. Zhu, Polymer microspheres for controlled drug release, *International Journal of Pharmaceutics*, Volume 282, Issues 1-2, 10 September 2004, Pages 1-18, ISSN 0378-5173, DOI: 10.1016/j.ijpharm.2004.04.013.
2. J A Jansen, et al, Injectable PLGA microsphere/calcium phosphate cements: physical properties and degradation characteristics, *Journal Of Biomaterials Science. Polymer Edition* 17.9 (2006): 1057-1074. MEDLINE with Full Text. EBSCO. Web. 14 Mar. 2011.
3. Jun Wang, J. Chen, J. Zong, D. Zhao, F. Li, R. Zhuo, S. Cheng, Calcium Carbonate/Carboxymethyl Chitosan hybrid microspheres and nanospheres for drug delivery, *J. Phys. Chem.* Vol. 114, No. 44, 2010.
4. Fu Yin Hsu, Shan-Chang Chueh, Yng Jiin Wang, Microspheres of hydroxyapatite/reconstituted collagen as supports for osteoblast cell growth, *Biomaterials* 20(1999), 1931-1936.
5. Habraken, W. J. E. M., de Jonge, L. T., Wolke, J. G. C., Yubao, L., Mikos, A. G. and Jansen, J. A.(2008), Introduction of gelatin microspheres into an injectable calcium phosphate cement. *Journal of Biomedical Materials Research Part A*, 87A: 643-655. Doi: 10.1002/jbm.a.31703
6. Hot Plate Stirrer: Best value Hot Plate Stirrer, 2007, The Lab Depot Inc, 16 April 2012. [http://www.labdepotinc.com/Product\\_Details~id~440~pid~13359.aspx](http://www.labdepotinc.com/Product_Details~id~440~pid~13359.aspx)
7. Bahukudumbi P, Carson K. H, Rice-Ficht A. C, Andrews M. J, On the diameter and size distributions of bovine serum albumin (BSA)-based microspheres, *Journal of Microencapsulation*, Volume 21, Number 7, November 2004, pp. 787-803
8. Foyeke O. Opawale, Diane J. Burgess, Influence of Interfacial Properties of Lipophilic Surfactants on Water-in-Oil Emulsion Stability, *Journal of Colloid and Interface Science*, Volume 197, Issue 1, 1 January 1998, Pages 142-150, ISSN 0021-9797, 10.1006/jcis.1997.5222.

# Exploration of the Relationship between Microscopic Structures and Macroscopic Properties of Biodiesel to Improve its Efficiency as a Future Energy Source

Joseph Imbrogno<sup>1</sup>, Sung Bong Tae<sup>1</sup>, Tadanori Koga<sup>1</sup>, Keith Jones<sup>2</sup>

<sup>1</sup>Department of *Materials Science and Engineering: Chemical and Molecular Engineering Program, Stony Brook University, NY 11794-2275*

<sup>2</sup>*Brookhaven National Laboratory, Upton, NY 11973-5000*

---

## Abstract

This research project was focused around studying the clouding point and gel point of soy and tallow based biodiesel. Therefore, the focus of our research was to study the structures present from the clouding point to the point when the biodiesel becomes a gel. Previous experiments have shown that a crystalline structure, in a bilayer structure, is formed upon clouding. The main technique used for analysis was wide angle x-ray scattering (WAXS) and FTIR was used briefly, but was not as useful as the x-ray data. Based on previous data, the clouding point of pure soy biodiesel is 38°F (~3°C) and 66°F (~19°C) for pure tallow biodiesel. Any number of new clouding points can be formed by mixing the two in different ratios. Samples of a 1:1 mixture of soy/tallow based biodiesel were studied. We were able to compare the expected clouding point from literature with the clouding point of our microscopic experiments to see if the results were consistent or, more interestingly, not consistent. X-ray scattering allowed us to see the transition points of our samples very clearly. Approximate  $q$  value peaks for the 1:1 mixture of soy and tallow were 15.6, 16.7, and 18.5 nm<sup>-1</sup>. We then determined an initial crystallization or transition point from the x-ray data by graphing intensity vs. temperature. The 1:1 soy/tallow mixture when heated showed two distinct Gaussian peaks from the WAXS data. The disappearance of these peaks indicated the transition point of the sample. The corresponding temperatures of these two values were 13.5°C (56.3°F) ± 0.5°C and 14.0°C (57.2°F) ± 0.5°C.

*Keywords:* Biodiesel, Soy, Tallow, Clouding point, Gel point, Wide angle x-ray scattering

---

## 1. Introduction

There has been great importance placed on developing an alternative energy source to decrease fuel costs and reduce our dependence on foreign oil. One such alternative source is biodiesel. A typical biodiesel is B100 fuel, which is made from different oil and fat sources. Since it is made from used fats and oils, it is composed of saturated and unsaturated fatty acid chains. These bonding differences are responsible for the different physical and combustion properties of the fuel. Saturated carbon chains have higher freezing points than unsaturated chains, which

have lower freezing points. Unsaturated chains have lower ignition quality (cetane number), lower fuel stability, and generate higher NO<sub>x</sub> submissions (Conley 2006). Some of these fuel properties can be seen in Table 1.

Another advantage to biodiesel is that it has a constant energy output regardless of its origin; regular diesel can vary up to 15% depending on its origin (Conley 2006).

Currently, biodiesel can be used during warm seasons of the year, but not when the temperature drops below the freezing point of the biodiesel mixture. This has been apparent when used in

**Table 1. Fuel Properties as a Function of Fuel Composition in Diesel Engines**

Chemical Property	Saturated 12:0, 14:0, 16:0, 18:0:0, 20:0, 22:0	Fatty Acids Monounsaturated 16:1, 18:1, 20:1, 22:1	Polyunsaturated 18:2, 18:3
Cetane Number	High	Medium	Low
Cloud Point	High	Medium	Low
Stability	High	Medium	Low
NO <sub>x</sub> Emissions	Reduction	Slight Increase	Large Increase

**Table 2. Cold Flow Properties for B100 Fuels**

B100 Fuel Type	Clouding Point (°F)	Pour Point (°F)	Cold Filter Plug Point (°F)
Soy methyl ester	38	25	28
Canola methyl ester	26	25	24
Lard methyl ester	56	55	52
Edible tallow methyl ester	66	60	58

internal combustion engines during cold weather. As stated above, the clouding point of pure soy biodiesel is 38°F (~3°C) and 66°F (~19°C) for pure tallow biodiesel. Other oils can be utilized for this process as well, as can be seen in Table 2.

Most research focuses on diesel fuel containing 2-20% biodiesel to improve cold flow (Chiu 2004). Various different techniques are employed to improve the flow of biodiesel in cold weather. Some of these techniques are: using additives like OS-110050, Bio Flow-870, etc. in order to reduce crystalline size (Chiu 2004), attach heating units, winterization to lower crystallization onset temperature (Dunn 1999), and blending to mix reagents with low freezing points and high combustion efficiency (Kralova 2010).

The initial onset of crystallinity is called the clouding point. The clouding point is used as a quality control specification. At the clouding point, saturated fatty acid esters form crystals and eventually make the fuel appear cloudy; continuous

agglomeration of crystals leads to clogging of fuel filter systems (Chuang-Wei Chiu 2004). Additives work by altering crystal size to avoid filter plugging, while blending is used to lower the clouding point. It has been shown previously that additives can reduce the pour point of biodiesel, specifically kerosene (Chuang-Wei Chiu 2004). When the proper additives are used, tank and fuel line heating systems can be averted.

Other characterization values of biodiesel are the pour point (PP), the cold filter plugging point (CFPP), and the low temperature flow test (LTFT). Since the cloud point (CP) and the pour point (PP) cannot predict operation temperatures, the CFPP and LTFT are utilized (Owen 1990). LTFT is considered the most reliable test because it is a dynamic test that simulates flow through filters. Biodiesel can clog filters with a crystalline size as small as 10 µm, which leads to fuel starvation and engine failure. Diesel fuel freezes at roughly -10 - -15°C, where soy-based biodiesel freezes at roughly 0°C (Chandler 1992). Another method of increasing efficiency of biodiesel production is at the source; i.e.: increasing initial production rate. Multiple previous experiments have indicated that after the first 60 minutes of conversion, about 85% of biodiesel is converted and only 5% is converted in the following 60 minutes; indicating chemical equilibrium (X. Meng 2008). At this equilibrium, glycerin can be separated from the biodiesel, earlier than it would usually be (Boni 2010). This allows for optimized refining because the process can begin earlier.

In contrast, this research focuses on mixtures with high concentrations of biodiesel; roughly 80-100%. Biodiesel is a renewable resource with readily available feedstock from multiple different sources, such as excess kitchen oils. The major issue, as stated above, is keeping flow rates up at low temperatures. A fundamental understanding of this problem will allow for the implementation of a preventative measure in order to stop clouding from occurring above a certain temperature. This will allow biodiesel to be used as a fuel year round and therefore will decrease the amount of petroleum based fuel that needs to be consumed.

Since both soy and tallow have different clouding points, mixing them produces a new intermediate clouding point; we want to determine the best mixture for our purposes that will produce the lowest clouding point. Ultimately, we want to effectively lower the clouding point by altering the biodiesel structure or using various different additives. This will allow biodiesel to be used in almost all temperature ranges.

## 2. Materials and Methods

### 2.1 Wide Angle X-ray Scattering

All WAXS experiments were done at the NSLS at Brookhaven National Laboratory in Upton, NY 11973-5000 on the X10A beam line. In short, the small cell was filled with less than one cm<sup>3</sup> of liquid biodiesel sample and exposed to the beam. The experiment was run by beam line personnel. The wavelength of the x-ray was 1.09 Å with a sample distance of 6.0 cm. Temperature control and data collection was done by us, which was controlled by a digital readout controller accurate to one decimal place. The temperature was typically varied from -10.0-25.0°C, at atmospheric pressure, stopping for approximately two minutes at every temperature interval to allow for stabilization. This temperature range was stepped in 0.5°C increments for both heating and cooling of the sample. The samples were heated and cooled in order to observe hysteresis if it was present (Cooling curves not shown).

### 2.2 Fourier Transform Infrared Spectroscopy

All FTIR experiments were done at the NSLS at Brookhaven National Laboratory in Upton, NY

11973-5000 on the U2B beam line. In short, the liquid sample, less than one cm<sup>3</sup>, was placed on a stage so it could be viewed under magnification. Liquid nitrogen was poured into the system by personnel that work at the beam line. The sample was then located using a viewfinder and joystick. The IR light was then directed onto the sample, producing readings on the screen. The temperature was then controlled using a digital readout controller. The temperature range was varied from -10.0-25.0°C, at atmospheric pressure, stopping for approximately two minutes at every temperature interval to allow for stabilization. This temperature range was stepped in 0.5°C increments for both heating and cooling the sample.

### 2.3 Wide Angle X-ray Scattering Data Analysis

The WAXS data was analyzed using XPolar and IGOR Pro software. The data was first converted to a file type that XPolar could read. Then, the wavelength, sample distance, and pixel size were input into a script along with the center of the x-ray image. Next, another script was used to integrate along the entire image and was then loaded into IGOR Pro. Plots of intensity vs.  $q$  (nm<sup>-1</sup>) were created by adding each data set corresponding to each temperature increment over the heating or cooling range. A theoretical curve was used to locate the peak intensities of each of the major peaks of the graphs. These peak intensities were then graphed against their corresponding temperatures in order to form a graph that showed the temperature at which the crystalline peaks appeared or disappeared. This process can be seen in Figure 1:

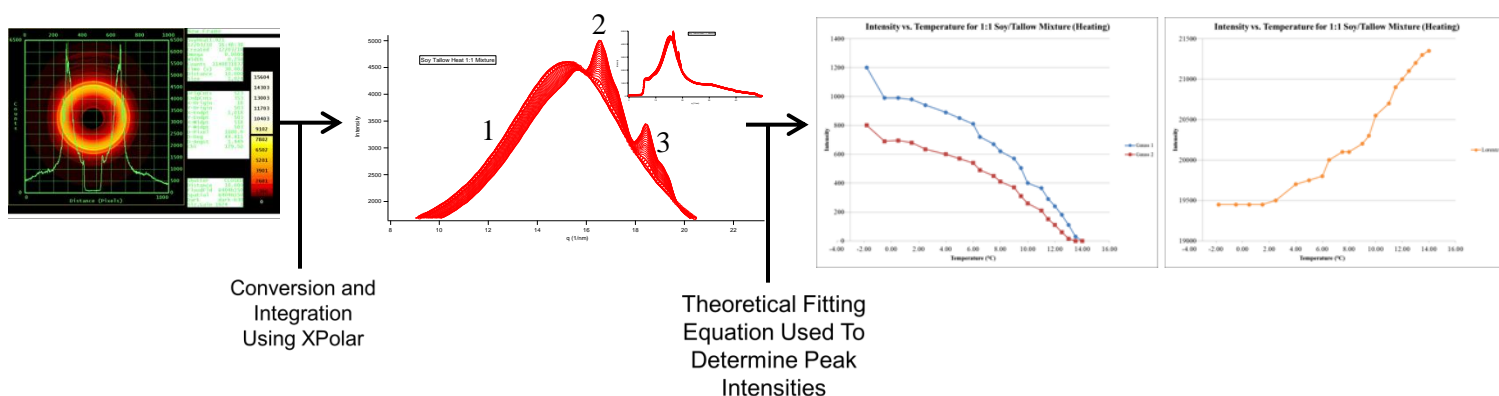


Figure 1. X-ray Data Analysis Process; where 1 = Lorentzian, 2 = Gaussian 1 (blue), 3 = Gaussian 2 (red)

### 3. Results and Discussion

After we graphed intensity vs. temperature (°C) we were able to get a better idea of when the onset of crystallization occurred (clouding point). This was then compared to a theoretical equation used to predict the clouding point of a mixture of two fuels. Fitting a mathematical equation to the data allowed us to do this. The clouding point that we found from the WAXS data deviated slightly from the theoretical clouding point. The same deviation was observed for the pure soy biodiesel data as well (not shown). The mathematical fitting equation can be seen in Equation 1:

Equation 1. Mathematical Equation Fit to Lorentzian-Gaussian-Gaussian Curves

$$f(x) = a_0 + a_1 / ((x - a_2)^2 + a_3) + a_4 * \exp(-((x - a_5) / a_6)^2) + a_7 * \exp(-((x - a_8) / a_9)^2)$$

Where:  $a_0$  = baseline;  
 $a_1, a_4, a_7$  = three peak intensities;  
 $a_2, a_5, a_8$  = three peak q values;  
 $a_3, a_6, a_9$  = three peak widths

A plot of peak intensity vs. temperature was generated for the 1:1 soy/tallow mixture. It can be seen in Figure 2 that each peak has a different temperature at which it becomes zero. This occurs when the lipid undergoes microscopic ordering as the

biodiesel passes through its clouding point. The two Gaussian peaks go through the phase transition at around the same temperature, from smallest to largest intensity; these transitions occurred at 13.5 and 14.0°C ± 0.5°C respectively. This range is also in between 3°C (38°F) and 19°C (66°F), which was expected based on the mixture. The Lorentzian peak is due to the intermolecular forces that are always present within the liquid sample; therefore, it increases as the sample returns to its liquid state after melting the crystals.

Based on prior research, an intermediate clouding point can be predicted when two samples of biodiesel are mixed together (Nowatzki 2012). The new clouding point can be determined linearly by Equation 2:

Equation 2. Intermediate Clouding Point Temperature from a Mixture

$$I_{CP} = (P_1 \times T_{CP1}) + (P_2 \times T_{CP2})$$

Where:  $P_n$  = Percent of fuel n;  
 $T_{CPn}$  = Clouding point of fuel n

Applying this formula to our sample, the theoretical clouding point should be 11°C (52°F). The WAXS data showed that the new clouding point was 14°C (57°F) ± 0.5°C, which is slightly higher than what the theoretical equation predicts. This difference could be due to error in the measurements taken, miscibility

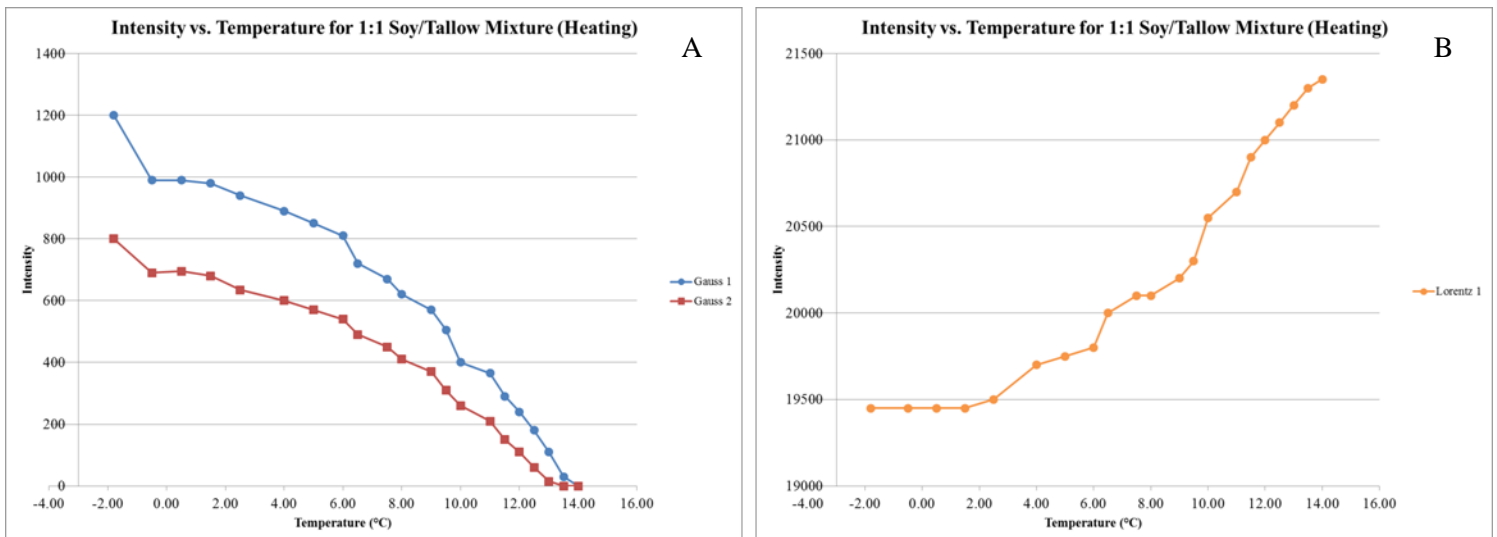


Figure 2. (A) Intensity vs. Temperature for Gaussian Peaks, (B) Intensity vs. Temperature for Lorentzian Peak

factors, it could be that the theoretical equation only predicts macroscopic clouding point; that is, the point at which clouding can be seen under visible light, or calibration error. We believe the latter is more likely, since the transition temperatures for the pure soy data also deviated by  $\sim 3^{\circ}\text{C}$ .

We propose that WAXS is able to predict the initial onset of crystalline structure formation, which is very close to the clouding point that can be observed by the naked eye under visible light. Since the x-ray data is based on very small measurements, nanometer scale, the clouding point predicted from the graph may actually occur slightly above the literature clouding point. As shown in Figure 2, it requires a large amount of small crystals to agglomerate before the group is big enough to show clouding under visible light.

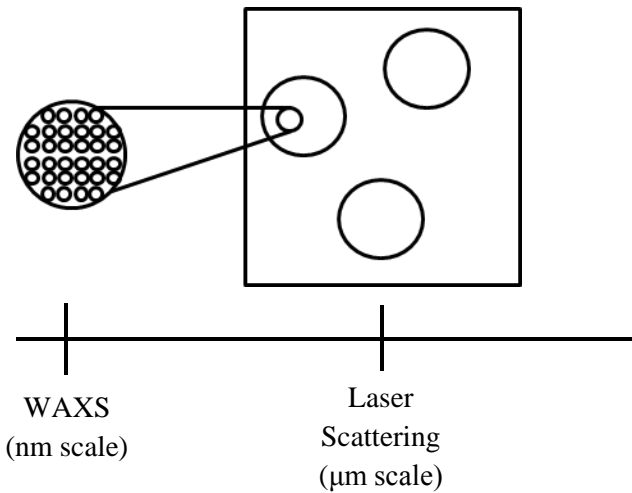


Figure 2. Proposed Model of Clouding Points Based on Size

Such a model fits our data because laser scattering would not be able to detect very small crystalline structures, while WAXS can.

Even though our experimental results did not match the theoretical equation exactly, it is still very likely that the transition temperature that was observed is in fact the clouding point transition temperature. A sketch of the major transitions can be seen in Figure 3.

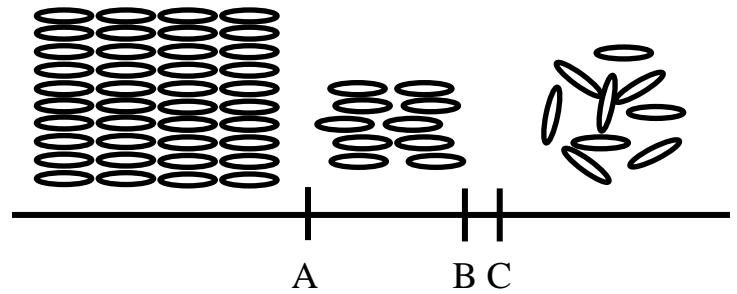


Figure 3. Transitions for 1:1 Soy/Tallow Biodiesel Mixture; where: (A) is  $T_{\text{gel}}$ , (B) is  $T_{\text{CP}}$  (literature), and (C) is  $T_{\text{trans}}$  (experimental)

The structure on the far right corresponds to the Lorentzian amorphous peak from the data which is present in the liquid. The sharp Gaussian peaks are due to the more ordered crystalline structure that begins to occur at the clouding point (B); or in our case, at the transition temperature (C). Once the biodiesel agglomerates a significant amount, it no longer flows well and behaves like a gel (A).

In future work, we would like to examine the WAXS data for different soy to tallow ratios to see if they also deviate from the theoretical equation and, if so, by how much. Laser light scattering tests for clouding point would be used to determine the macroscopic clouding point of the blend in order to have a standard clouding point to be used in the equation. If the same deviation occurs, we would be able to determine if this new transition temperature has physical significance. It would also be useful to perform these experiments using different biodiesels, such as canola or lard. Then we could compare their clouding points to the other mixtures as well as to their literature and predicted clouding points.

## References

1. Boni, L. A. B. D. (2010). "Monitoring the Transesterification Reaction with Laser Spectroscopy." Fuel Processing Technology **92**(5): 1001-1006.
2. Chandler, J. E. a. F. G. H. (1992). "The Effect of Cold Flow Additives on Low-Temperature Operability of Diesel Fuels." SAE Technical Paper Series **922186**.
3. Chiu, C.-W. (2004). "Impact of Cold flow improvers on soybean biodiesel blend." Biomass and Bioenergy **27**: 485-491.
4. Chuang-Wei Chiu, L. G. S., Galen J. Suppes (2004). "Impact of Cold flow improvers on soybean biodiesel blend." Biomass and Bioenergy **27**(5): 485-491.
5. Conley, S. P. (2006) Biodiesel Quality: Is All Biodiesel Created Equal? Bioenergy
6. Dunn, R. (1999). "Thermal Analysis of Alternative Diesel Fuels from Vegetable Oils." JAOCS **76**(1).
7. Kralova, I. (2010). "Biofuels–Renewable Energy Sources: A Review." Journal of Dispersion Science and Technology **31**: 409-425.
8. Nowatzki, J. (2012) Biodiesel Cloud Point and Cold Weather Issues. Cornell University Cooperative Extension
9. Owen, K. a. T. C. (1990). "Diesel Fuel Low-Temperature Characteristics." Automotive Fuels Handbook: 353-403.
10. X. Meng, G. C., Y. Wang (2008). "Biodiesel production from waste cooking oil via alkali catalyst and its engine test." Fuel Process Tech **89**: 851-857.